

Distributions of Shallow to Very Deep Precipitation–Convection in Rapidly Intensifying Tropical Cyclones

CHENG TAO AND HAIYAN JIANG

Department of Earth and Environment, Florida International University, Miami, Florida

(Manuscript received 20 June 2014, in final form 12 July 2015)

ABSTRACT

Shear-relative distributions of four types of precipitation/convection in tropical cyclones (TCs) are statistically analyzed using 14 years of Tropical Rainfall Measuring Mission (TRMM) Precipitation Radar (PR) data. The dataset of 1139 TRMM PR overpasses of tropical storms through category-2 hurricanes over global TC-prone basins is divided by future 24-h intensity change. It is found that increased and widespread shallow precipitation (defined as where the 20-dBZ radar echo height <6 km) around the storm center is a first sign of rapid intensification (RI) and could be used as a predictor of the onset of RI. The contribution to total volumetric rain and latent heating from shallow and moderate precipitation (20-dBZ echo height between 6 and 10 km) in the inner core is greater in RI storms than in non-RI storms, while the opposite is true for moderately deep (20-dBZ echo height between 10 and 14 km) and very deep precipitation (20-dBZ echo height ≥ 14 km). The authors argue that RI is more likely triggered by the increase of shallow–moderate precipitation and the appearance of more moderately to very deep convection in the middle of RI is more likely a response or positive feedback to changes in the vortex. For RI storms, a cyclonic rotation of frequency peaks from shallow (downshear right) to moderate (downshear left) to moderately and very deep precipitation (upshear left) is found and may be an indicator of a rapidly strengthening vortex. A ring of almost 90% occurrence of total precipitation is found for storms in the middle of RI, consistent with the previous finding of the cyan and pink ring on the 37-GHz color product.

1. Introduction

Prediction of tropical cyclone (TC) intensity change, especially rapid intensification (RI), has shown relatively little improvement over the last three decades compared with forecasts of TC motion, in spite of the availability of advanced satellite observations and the development of sophisticated numerical models. One of the most fundamental reasons is a lack of understanding of the physical processes and mechanisms that govern the TC intensity variability.

Intensity forecasting is challenging since the inner-core evolution involves a complex interaction among processes occurring on spatial scales varying over many orders of magnitude (Marks and Shay 1998). Several environmental conditions associated with RI have been identified, including warm sea surface temperatures

(SSTs) and a deep warm oceanic mixed layer, low vertical wind shear, high lower-tropospheric relative humidity, conditional instability, large-scale upper-level divergence, and low-level convergence patterns (Merrill 1988; Kaplan and DeMaria 2003; Wang and Wu 2004). Although these environmental and oceanic factors are reasonably well predicted owing to improvements in dynamical models and have proved to be useful in forecasting RI (Kaplan et al. 2010), the false-alarm ratio still remains undesirably high, suggesting that these external processes play only a partial role in RI. It is thus reasonable to hypothesize that internal processes operating on scales smaller than the environmental scales may be much more important in distinguishing RI and slowly intensifying storms (Hendricks et al. 2010).

Convective-scale processes within the inner-core region of TCs are widely believed to be one of the most important subsynoptic-scale contributors to TC intensification. Previous modeling studies have argued the importance of rotating, asymmetric deep convection in the inner core, termed vortical hot towers (VHTs), to TC intensification (Hendricks et al. 2004; Montgomery

Corresponding author address: Dr. Haiyan Jiang, Department of Earth and Environment, Florida International University, AHCS Rm 371, 11200 SW 8th Street, Miami, FL 33199.
E-mail: haiyan.jiang@fiu.edu

et al. 2006; Nguyen et al. 2008). Montgomery and Smith (2011) proposed that asymmetric convection/heating was the preferred spinup mechanism. However, it is noted that these VHTs were mainly reported in tropical depressions by observational studies (e.g., Reasor et al. 2005; Houze et al. 2009), while RI usually occurs in storms ranging in intensity from tropical storms through category-2 hurricane systems (Kaplan and DeMaria 2003; Kieper and Jiang 2012).

In contrast, many early theoretical studies have shown that symmetric convection/heating was the preferred mechanism at spinning up the inner-core winds (e.g., Ooyama 1969; Shapiro and Willoughby 1982). More recently, Nolan and Grasso (2003) and Nolan et al. (2007) revisited the issue and examined the evolution of a symmetric, balanced vortex perturbed by asymmetric, unbalanced heat sources based on an improved linearized primitive equation model. They indicated that the intensity of the vortex changes as a symmetric response to the azimuthally averaged latent heating release and found that heating inside the radius of maximum winds (RMW) has a much higher efficiency with which diabatic heating released within the storm core is converted into the kinetic energy of the storm-scale primary circulation (e.g., Vigh and Schubert 2009; Rogers 2010). This suggests that asymmetric, intense convective cells (e.g., hot towers) do not play any specific role in intensification other than to the extent to which they add to the symmetric mean heating.

Particularly for RI, several observational case studies have shown horizontally small-scale, asymmetric deep convection (such as convective bursts and hot towers) within the inner core of TCs undergoing RI (Reasor et al. 2009; Guimond et al. 2010; Molinari and Vollaro 2010; Nguyen and Molinari 2012; Reasor and Eastin 2012; Stevenson et al. 2014; Rogers et al. 2015; Susca-Lopata et al. 2015), especially when the storm was experiencing moderate-to-high vertical wind shear. For example, Nguyen and Molinari (2012) argued that Hurricane Irene (1999) rapidly intensified because the diabatic heating produced by asymmetric, intense convection was strong enough to dramatically increase the azimuthally averaged heating. Reasor et al. (2009) and Reasor and Eastin (2012) illustrated that the rapid intensification of Hurricane Guillermo (1997) under moderate shear coincided with the formation and cyclonic rotation of strong convective bursts through the left-of-shear semicircle. A series of observational studies on Hurricane Earl (2010) (Stevenson et al. 2014; Rogers et al. 2015; Susca-Lopata et al. 2015) showed that asymmetric deep convective bursts and lightning strikes occurred before Earl's rapid intensification.

However, statistical studies using long-term satellite observations have shown different results. To test the

VHT theory hypothesized by modeling studies (e.g., Montgomery and Smith 2011), Jiang (2012) examined the inner-core convection, especially hot towers (defined as maximum 20-dBZ radar echo height ≥ 14.5 km), in different TC intensity change categories. It was shown that the probability of 24-h future RI does not significantly increase when hot towers exist in the inner-core region, and it was suggested that hot towers are neither a necessary nor a sufficient condition for RI. Several other satellite-based statistical studies supported the symmetric mechanism of TC intensification with a focus on RI. Kieper and Jiang (2012) indicated that a symmetric ring feature on the Naval Research Laboratory (NRL) 37-GHz color composite microwave satellite product (Lee et al. 2002) is a very good predictor of RI in the following 24 h. They subjectively defined the ring to be at least 90% closed around the storm center with either cyan color or pink color on the NRL 37-GHz color product. Lee et al. (2002) indicated that qualitatively warm rain or low-level water clouds appear cyan and deep convection appears pink. However, by reviewing a large number of TRMM TC overpasses, we found that any precipitation with ice aloft appears pink, which could be either stratiform or convective, and not necessarily deep convection. Although it is often claimed that the ring is "precipitative" (Zagrodnik and Jiang 2014, hereafter ZJ14), it has never been proven with direct quantitative information. As an indirect proof, using a 10-yr dataset from the Tropical Rainfall Measuring Mission (TRMM) satellite, Jiang and Ramirez (2013) determined that RI in the future 24 h requires a minimum threshold for the current inner-core raining area and volumetric rain that is appreciably higher than non-RI storms.

By compositing a large number of passive microwave satellite overpasses relative to vertical wind shear direction, Harnos and Nesbitt (2011) claimed that they found a convective ring forming 6 h before RI begins and intensifying over the following 24-h RI period. The ring at the onset of RI had a 50% occurrence of an ice-scattering signature defined by the 85-GHz polarization-corrected brightness temperature (PCT; Spencer et al. 1989) < 250 K, indicating at least moderate convection in TC eyewalls with TRMM PR 17-dBZ radar echo-top heights around 9–10 km (Cecil and Zipser 2002, their Fig. 10). However, Harnos and Nesbitt's (2011) study did not mirror the Southern Hemisphere TC overpasses relative to shear direction before compositing them with Northern Hemisphere TC overpasses. This could cause a severe overestimate of the percent occurrence of convection, especially in the right-of-shear quadrants. Indeed, Harnos and Nesbitt's (2011) Fig. 3 showed that the occurrence of 85-GHz PCT ≤ 250 K is downshear-right dominant during RI, RI + 6 h, and RI + 12 h, which

is contradictory to many previous studies that have confirmed the downshear-left regions as the preferred regions for total precipitation and convection (Corbosiero and Molinari 2002, 2003; Chen et al. 2006; Cecil 2007; Hence and Houze 2012).

A more careful study, conducted by ZJ14, composited the 14 years of TRMM Precipitation Radar (PR) overpasses only from Northern Hemisphere TCs. Not surprisingly, they showed a ring of only 5% occurrence of radar reflectivity >20 dBZ at or above 10-km elevation, which is a moderately intense convection definition slightly stronger than that used in Harnos and Nesbitt (2011), for storms that have undergone RI for at least 12 h and will continue to rapidly intensify during the following 24 h (see their Fig. 8e). Although ZJ14 were not able to directly prove that the 37-GHz cyan and pink ring found by Kieper and Jiang (2012) is precipitative, ZJ14's Fig. 6e does show a closed ring of 70% occurrence of near-surface PR reflectivity >20 dBZ for storms that have undergone RI for at least 12 h and will continue to rapidly intensify during the following 24 h. Note that the 20-dBZ level is closely analogous to the raining area and was used to define precipitation features in Nesbitt et al. (2000). Because of the larger footprint size of the 37-GHz channel than that of the PR, it is highly possible that a ring at a larger percent occurrence would be seen if the PR data used in ZJ14 were degraded to the 37-GHz equivalent footprint size. ZJ14 concluded that the rainfall frequency and latent heating distributions were more symmetric near the onset of RI and continued to be more symmetric as RI continues and the rainfall coverage expands upshear.

While these satellite-based statistical studies implied that the symmetry of widespread precipitation containing a much lower percentage of asymmetric deep convection is important in initiating RI in the following 24 h, observational case studies mentioned above (Reasor et al. 2009; Guimond et al. 2010; Molinari and Vollaro 2010; Nguyen and Molinari 2012; Reasor and Eastin 2012; Stevenson et al. 2014; Rogers et al. 2015) emphasized the role of asymmetric very deep convection in RI. An important question raised from this is, what is the relative importance of precipitation–convection of different depths–intensities to RI? In this study, we consider the inner-core precipitation–convection in more detail by separating it into four categories according to its radar echo-top height from very deep, moderately deep, moderate, to shallow. The latent heat release in the inner core is the primary driving force of TC intensification. ZJ14 found that total rainfall amount is closely correlated with total latent heat release, and the rainfall frequency is best correlated to future intensity change. In this study, we focus specifically on the frequency of four kinds of

precipitation–convection and their corresponding contribution to total volumetric rain in different TC future 24-h intensity change stages. Our primary goal is to identify whether there are significant differences in the distributions of different kinds of inner-core precipitation–convection between storms at the beginning of RI, the middle of RI, and those that do not undergo RI. We also focus on quantifying the relative contribution to total volumetric rain in the inner core from moderately deep–very deep convection versus shallow–moderate precipitation.

This study extends ZJ14's work by using an extended version of their TRMM PR dataset that exclusively includes storms in at least moderately favorable environments (see section 2a). ZJ14 focused on the distributions of rainfall frequency, moderately deep convection, and latent heating, while this study focuses on the frequency of four types of precipitation–convection and their relative contributions to total rainfall. Similar to ZJ14, we consider the distribution of precipitation–convection relative to the TC center and relative to the vertical wind shear. The organization of TC convection and precipitation within the inner core is primarily dominated by the environmental vertical wind shear, while the impact of storm motion on the eyewall convective asymmetry appears to be secondary (Corbosiero and Molinari 2002, 2003; Reasor et al. 2013). Both numerical model simulations (e.g., Rogers et al. 2003) and observational studies (Corbosiero and Molinari 2002, 2003; Chen et al. 2006; Cecil 2007; Hence and Houze 2012) have confirmed that the downshear to downshear-left regions are favored for upward motion and precipitation.

The TRMM spectral latent heating (SLH) estimates (Shige et al. 2004, 2007) were analyzed intensively in ZJ14. In this study, we analyze both latent heating and total rainfall, but results shown below focus mainly on total rainfall. As pointed out by Park and Elsberry (2013), the SLH algorithm significantly underestimates convective-scale cooling rates in tropical mesoscale convective systems. Therefore, the latent heating results in both ZJ14 and this study likely overestimate the heating rates at lower levels in convective pixels.

2. Data and methodology

a. TRMM PR overpasses selection

The dataset used in this study is an extended version of the 14-yr TRMM PR dataset (from 1998 to 2011) used by ZJ14. ZJ14's dataset is derived from the TRMM Tropical Cyclone Precipitation Feature database (TCPF; Jiang et al. 2011). TCPF includes the overpasses of all global TCs viewed by the TRMM satellite that reached

tropical storm intensity during their lifetimes. The storm center, storm intensity, and storm translation speed of each overpass are interpolated from the National Hurricane Center (NHC) and Joint Typhoon Warning Center (JTWC) best-track data. As the PR has a narrow 247-km swath (215 km before the TRMM orbital boost in August 2001), ZJ14 have manually filtered all PR overpasses so that at least some portion of the TC center or near-center area is within the PR swath. The best-track storm center of each overpass was also manually adjusted by ZJ14 when the PR or TRMM Microwave Imager (TMI) 37-GHz data suggest that the center should be moved. Geographically, overpasses used in ZJ14 were restricted to the Northern Hemisphere, including the Atlantic, North Pacific (eastern and western), and north Indian Ocean basins. In this study, overpasses in the Southern Hemisphere (including south Indian and South Pacific Ocean basins) are also included. We use version 7 of the TRMM PR 2A25 algorithm (Iguchi et al. 2009) reflectivity and rain rate and 2H25 latent heating data (Shige et al. 2007). As indicated by ZJ14, 2H25 latent heating is closely correlated with PR 2A25 rain rates with a linear correlation coefficient of 0.89. The PR reflectivity has a vertical resolution of approximately 250 m (at nadir) and a horizontal resolution of $5 \times 5 \text{ km}^2$ ($4.3 \times 4.3 \text{ km}^2$ before the orbital boost). To compare the 37-GHz cyan and pink ring with the radar reflectivity and 85-GHz PCT field, the TMI 1B11 37- and 85-GHz brightness temperatures are also used in this study.

It is well known that RI rarely occurs in an unfavorable environment, such as during movement to a region with cold SST or strong vertical wind shear, or during landfall (Kaplan and DeMaria 2003). To focus on the role of inner-core convection in RI, ZJ14 have applied several criteria to the selection of PR overpasses to exclude the impacts of both external factors and other internal factors, such as eyewall replacement cycles (Willoughby et al. 1982). These criteria are as follows: SST $> 26^\circ\text{C}$, vertical wind shear $< 16 \text{ m s}^{-1}$, mean inner-250-km total precipitable water (TPW) $> 50 \text{ mm}$, storm translation speed $< 11 \text{ m s}^{-1}$, the TC center is located over water both at the time of the overpass and 24 h in the future, and the intensity of the storm at the time of the overpass is between tropical storm and category-2 hurricane. According to ZJ14, the cutoff criteria for SST, TPW, shear, and storm motion were derived from a larger dataset of several thousand TRMM TMI overpasses. All storms that underwent RI in that larger dataset had environmental conditions that met or exceeded these minimum criteria. The SST is derived from the 0.25° resolution Reynolds daily SST grid point nearest to the storm center (Reynolds et al. 2007). The

TABLE 1. Definition of intensity change categories and sample size of selected PR overpasses for each category. The quantities V_{max} and $V_{\text{max}+24}$ represent the current and future 24-h maximum surface wind speeds ($1 \text{ kt} \approx 0.51 \text{ m s}^{-1}$), respectively.

| Category | 24-h future max wind speed change range (kt) | No. of PR overpasses |
|----------|---|-------------------------|
| W | $V_{\text{max}+24} - V_{\text{max}} \leq -10$ | 191 |
| N | $-10 < V_{\text{max}+24} - V_{\text{max}} < 10$ | 449 |
| SI | $10 \leq V_{\text{max}+24} - V_{\text{max}} < 30$ | 360 |
| RI | $V_{\text{max}+24} - V_{\text{max}} \geq 30$ | 139 |
| Total | | 1139 |

vertical wind shear is calculated by averaging the 200- and 850-hPa wind vectors from the European Centre for Medium-Range Weather Forecasts (ECMWF) interim reanalysis dataset (Simmons et al. 2007) within a ring of 500–750 km from the TC center and subtracting the averaged 200-hPa wind vector from the averaged 850-hPa wind vector. The 500–750-km ring is used to eliminate the influence of the storm's circulation as much as possible by following the method of Hense and Houze (2011). The TPW data from the ECMWF has a resolution of $0.75^\circ \times 0.75^\circ$ and was averaged for the innermost 250 km around the TC center. More details of the dataset are described by ZJ14.

b. Selection of intensity change categories

The final dataset contains a total of 1139 PR TC overpasses from 489 storms in global TC-prone basins between 1998 and 2011. In this study, the intensity of a TC is defined as the maximum sustained surface wind. Based on the difference in the maximum surface wind between the time of the overpass and 24 h in the future, all overpasses are classified into four intensity change categories: weakening (W), neutral (N), slowly intensifying (SI), and rapidly intensifying (RI), following the method of Jiang (2012) and Jiang and Ramirez (2013). Table 1 lists definitions and final sample sizes in each category. It should be noted that the RI definition in Table 1 depends only on the difference between the current and future 24-h intensity. However, an RI event (defined as multiple, continuous, and overlapping 24-h periods in which the intensity increased in each period by 30 kt or more; see Kieper and Jiang 2012) can continue for as long as 48–60 h. This indicates that the time of the overpasses in the RI category does not necessarily correspond to the onset of the RI event. Therefore, based on the intensity change in the 12, 18, and 24 h prior to the TRMM overpass, RI cases are subdivided into RI initial and RI continuing by following ZJ14. The RI initial storms began an RI event within 12 h of the overpass, while the RI continuing storms had a previous 24-h RI period beginning at 12, 18, or 24 h prior to the

TABLE 2. Definition of initial and continuing RI and the number of sampled PR overpasses.

| Category | Max wind speed range (kt) | PR overpasses | Passes with a 85-GHz PCT ≤ 250 K ring | Passes with a 37-GHz cyan and pink ring | Passes with a 37-GHz ring within PR swath |
|---------------|--|---------------|--|---|---|
| RI initial | $V_{\max+24} - V_{\max} \geq 30$ and $V_{\max}(0, +6, +12) - V_{\max}(-24, -18, -12) < 30$ | 59 | 5 | 42 | 30 |
| RI continuing | $V_{\max+24} - V_{\max} \geq 30$ and $V_{\max}(0, +6, +12) - V_{\max}(-24, -18, -12) < 30$ | 80 | 23 | 70 | 53 |
| RI total | $V_{\max+24} - V_{\max} \geq 30$ | 139 | 28 | 112 | 83 |

overpasses. It is important to note that the RI event in both subcategories continues for at least 24 h following the overpass. Therefore, both subcategories are important in the forecast of RI, although the RI initial storms are near the onset of an RI event, while the RI continuing storms are in the middle of an RI event. The definition and the corresponding sample sizes of RI initial and RI continuing overpasses are summarized in Table 2. There are 59 out of 139 RI overpasses (42%) during which the storms did not rapidly intensify (>30 kt per 24 h increase) in the past 12, 18, or 24 h, therefore being categorized as RI initial.

Figure 1 displays the frequency distributions of initial intensity, intensity change during the past 12 h, SST, TPW, environmental vertical wind shear, and storm motion for different intensity change categories. The corresponding means are summarized in Table 3. Student's t tests show that RI continuing storms have higher initial intensity and lower environmental shear than RI initial storms, which are significant at the 99.9% and 95% confidence levels, respectively. However, the differences of the two parameters between SI and RI initial storms, and the differences of all other parameters among various TC intensity change categories, are not significant at any confidence level. This indicates that, under minimally favorable environmental conditions, it is difficult to predict RI based on the environment alone.

c. Definition of four kinds of precipitation–convection

Hot towers have been defined in many ways, with cloud-top brightness temperatures colder than a given threshold from satellite infrared (IR) images (e.g., Gettelman et al. 2002; Jiang and Tao 2014), extremely low PCT (e.g., Spencer et al. 1989) measured by microwave radiometers owing to the large amount of frozen hydrometeors, high radar reflectivity at high altitude (e.g., Kelley et al. 2004; Liu and Zipser 2005; Tao and Jiang 2013; Jiang and Tao 2014), or strong mean upward motion within the midtroposphere (e.g., Rogers 2010; Reasor et al. 2009). In this study, very deep precipitation (i.e., a hot tower) is defined as the 20-dBZ radar echo height ≥ 14 km, consistent with Tao and

Jiang (2013) and Jiang and Tao (2014). A better name would be “very deep convection.” However, different types of precipitation–convection are defined using the height of 20-dBZ radar echo in this study. For pixels with higher echo-top heights, they are more likely to be convection (or convective precipitation). But for lower echo tops, they could be either convective or stratiform precipitation. In any case, the 20-dBZ radar echo indicates precipitating clouds. Therefore, in the following text, the name of each type of precipitation–convection is referred to as precipitation instead of convection, although it might be more appropriate to refer to the very deep and moderately deep types as convection.

To further examine the relative importance of very deep precipitation versus shallow–moderate precipitation in initiating RI, three more types of precipitation are identified based on the height of 20-dBZ radar echo ($Z_{20\text{dBZ}}$), including moderately deep precipitation ($14 > Z_{20\text{dBZ}} \geq 10$ km), moderate precipitation ($10 > Z_{20\text{dBZ}} \geq 6$ km), and shallow precipitation ($Z_{20\text{dBZ}} < 6$ km). At the top of the cloud, the radar reflectivity is approximately 20 dBZ (note that the PR's minimum detectable signal is about 17 dBZ), which corresponds to a precipitation rate of approximately 1 mm h^{-1} of ice hydrometeors (Kelley 2008). Here we use the height of the 20-dBZ radar echo as a proxy for convective/precipitative intensity.

The hot tower hypothesis proposed that tall convective clouds with undiluted cores play important roles in heat and moisture transport between the upper troposphere and lower stratosphere (Riehl and Malkus 1958; Simpson 1978). A recent study by Fierro et al. (2009), however, indicated that the cores that transport a considerable amount of moist static energy were diluted by entrainment. From their model simulations, over 60% of the air parcels originating near cloud base penetrated over 10-km altitude, while only 5% exceeded the 14-km level. Thus, it was suggested that the definition of hot towers be redefined as deep convective clouds that reach 10 km or above, the upper levels of the troposphere. Although Fierro et al.'s (2009) study was of a convective line in the Tropical Ocean and Global Atmosphere Coupled Ocean–Atmosphere Response Experiment (TOGA COARE)

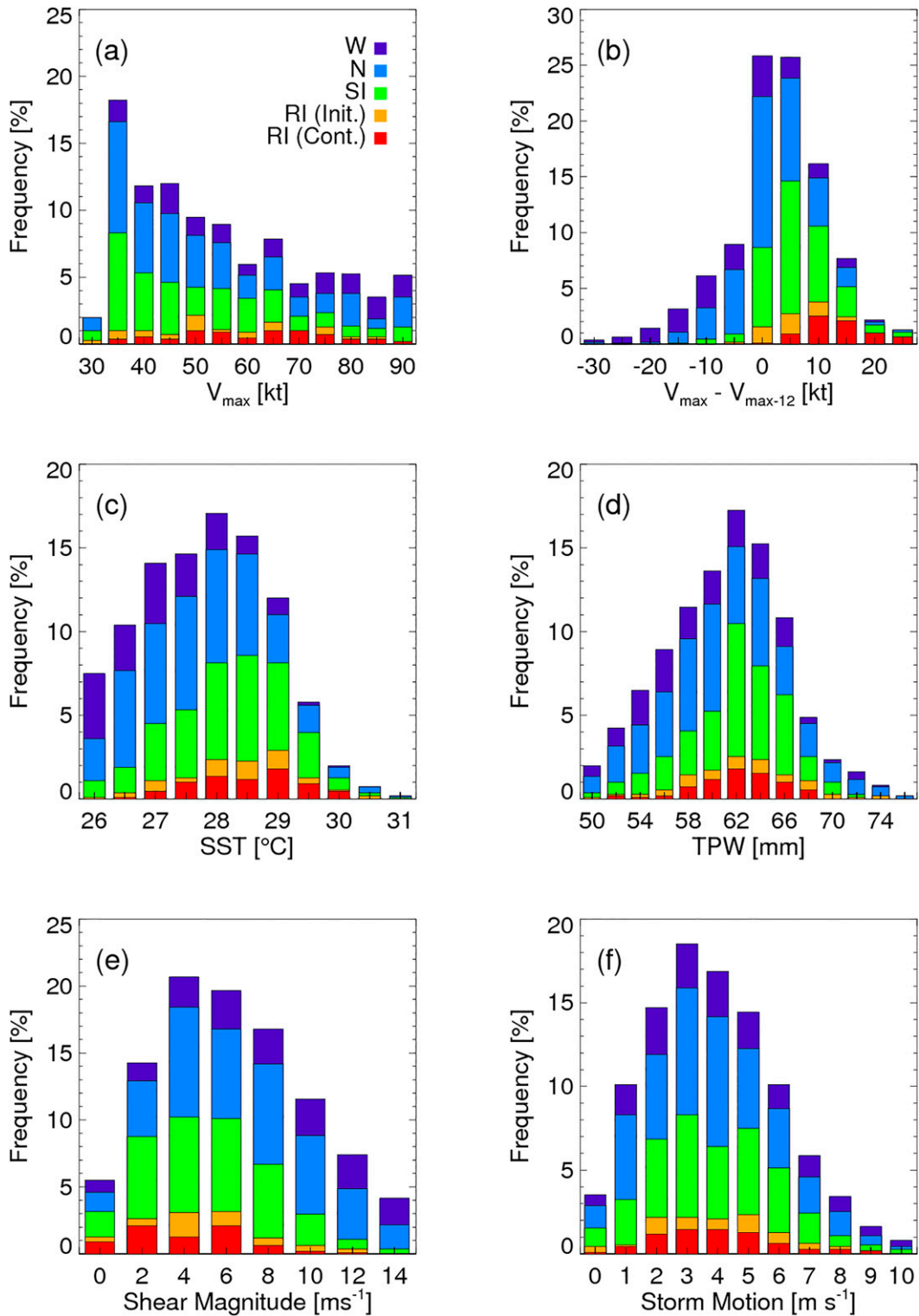


FIG. 1. Frequency distribution of (a) maximum sustained surface wind speed intensity (V_{\max}) at the time of the TRMM overpass, (b) the change of V_{\max} during the 12 h before the overpass, (c) SST, (d) TPW, (e) shear magnitude, and (f) storm motion. Each distribution is divided into colors representing the five future 24-h intensity change categories shown in (a).

TABLE 3. Mean values of current V_{\max} , the change of V_{\max} during the 12 h before the overpass, SST, TPW, vertical wind shear magnitude, storm motion, and the difference in the direction of the vertical wind shear and the storm motion vector parameters for the total dataset and different intensity change categories. Asterisks in the RI, RI initial, and RI continuing columns represent the statistical significance between SI and RI, SI and RI initial, and RI initial and RI continuing storms, respectively, at the 90% (*), 95% (**), 99% (***), and 99.9% (****) confidence levels.

| Mean values | W | N | SI | RI | RI initial | RI continuing | Total |
|-------------------------------|-------|-------|-------|----------|------------|---------------|-------|
| V_{\max} (kt) | 63.5 | 53.8 | 52.6 | 60.4**** | 56.1 | 63.4**** | 55.9 |
| $V_{\max} - V_{\max-12}$ (kt) | -2.7 | 2.8 | 8.0 | 12.1 | 7.0 | 15.7 | 4.6 |
| SST ($^{\circ}\text{C}$) | 27.4 | 28.0 | 28.4 | 28.7 | 28.6 | 28.7 | 28.1 |
| TPW (mm) | 60.6 | 61.7 | 62.9 | 63.3 | 63.5 | 63.2 | 62.1 |
| Shear (m s^{-1}) | 8.9 | 7.9 | 6.3 | 5.5** | 6.3 | 5.0** | 7.3 |
| Motion (m s^{-1}) | 4.6 | 4.2 | 4.4 | 4.5 | 4.5 | 4.4 | 4.4 |
| Shear - motion ($^{\circ}$) | -60.5 | -53.1 | -55.5 | -61.7 | -51.0 | -69.7 | -56.2 |

and not associated with a TC, other studies also suggested that the 17–20-dBZ radar echo reaching 10 km is a good criterion for moderately intense convection in TCs (e.g., Cecil and Zipser 2002; ZJ14). Based on these studies, the 10-km level is selected to separate moderate and moderately deep precipitation–convection. The very deep precipitation and moderately deep precipitation categories collectively are equivalent to the redefined hot towers as proposed by Fierro et al. (2009).

To examine the contribution of latent heat energy attributable to liquid precipitation versus ice processes, the 6-km altitude is chosen to separate shallow and moderate precipitation. In the inner core of TCs, the freezing level is close to 5 km (Hence and Houze 2011) and perhaps higher than 5 km for more intense storms. Therefore, it is reasonable to assume that there is almost no ice in the inner core below 6 km. Even if there is some small amount of ice, results in this study focus more on the depth of the precipitation and latent heat release than on microphysics.

d. Methodology and selection of variables

This study uses two types of figures: radial distributions and two-dimensional (2D) composite images. The radial distribution plots are generated by grouping the PR pixels from different intensity change categories into bins representing 5-km annuli extending radially outward from the TC center. The 2D composite images are chosen for their advantage of allowing for the accumulation of data from numerous overpasses in a single 2D plot to display the shear-directed distributions of precipitation in TCs. To generate a composite image, the PR overpasses are first rotated with the vertical wind shear vector pointing northward (along the +y axis) and the TC center located in the center of the plot. The shear-relative pixels of Southern Hemisphere overpasses are flipped 180° before compositing them with Northern Hemisphere cases, following Chen et al. (2006) and Wingo and Cecil (2010). The PR pixels, with

their new coordinates relative to the TC center and vertical wind shear vector, are then compiled into $10 \times 10 \text{ km}^2$ grid cells. As a result, the value of each grid cell represents either the frequency or total volumetric rain (see selection of variables in the next paragraph) of pixels satisfying each precipitation type criterion relative to total pixels that fall into each 100 km^2 box. It is noted that both RI and very deep precipitation are rare events. To ensure meaningful statistics when generating the composites, we require that at least three PR pixels meet the precipitation criterion within each 100-km^2 box from all overpasses for each intensity change category.

As described in the introduction, our main goal is to examine the frequency of four kinds of precipitation and their corresponding contribution to total volumetric rain and latent heating in different TC future 24-h intensity change stages. Therefore, three variables are selected for this study: 1) percent occurrence of each type of precipitation (%), 2) total volumetric rain ($\text{mm h}^{-1} \text{ km}^2$), and 3) total latent heating (K h^{-1}). The percent occurrence of precipitation is the fraction of the number of pixels from different types of precipitation divided by the total number of PR pixels. The total volumetric rain is the sum of the pixel-based products of multiplying the PR 2A25 near-surface rain rate (mm h^{-1}) by the area of each pixel within each annulus or grid cell normalized by the number of pixels in the domain. The total latent heating is the sum of vertically integrated PR 2H25 latent heating from the surface to 18 km within each annulus or grid cell normalized by the number of pixels in the domain, following ZJ14.

3. Results

a. Percent occurrence of precipitation

1) RADIAL DISTRIBUTIONS

Figure 2 shows the radial distributions of percent occurrence of four kinds of precipitation and total

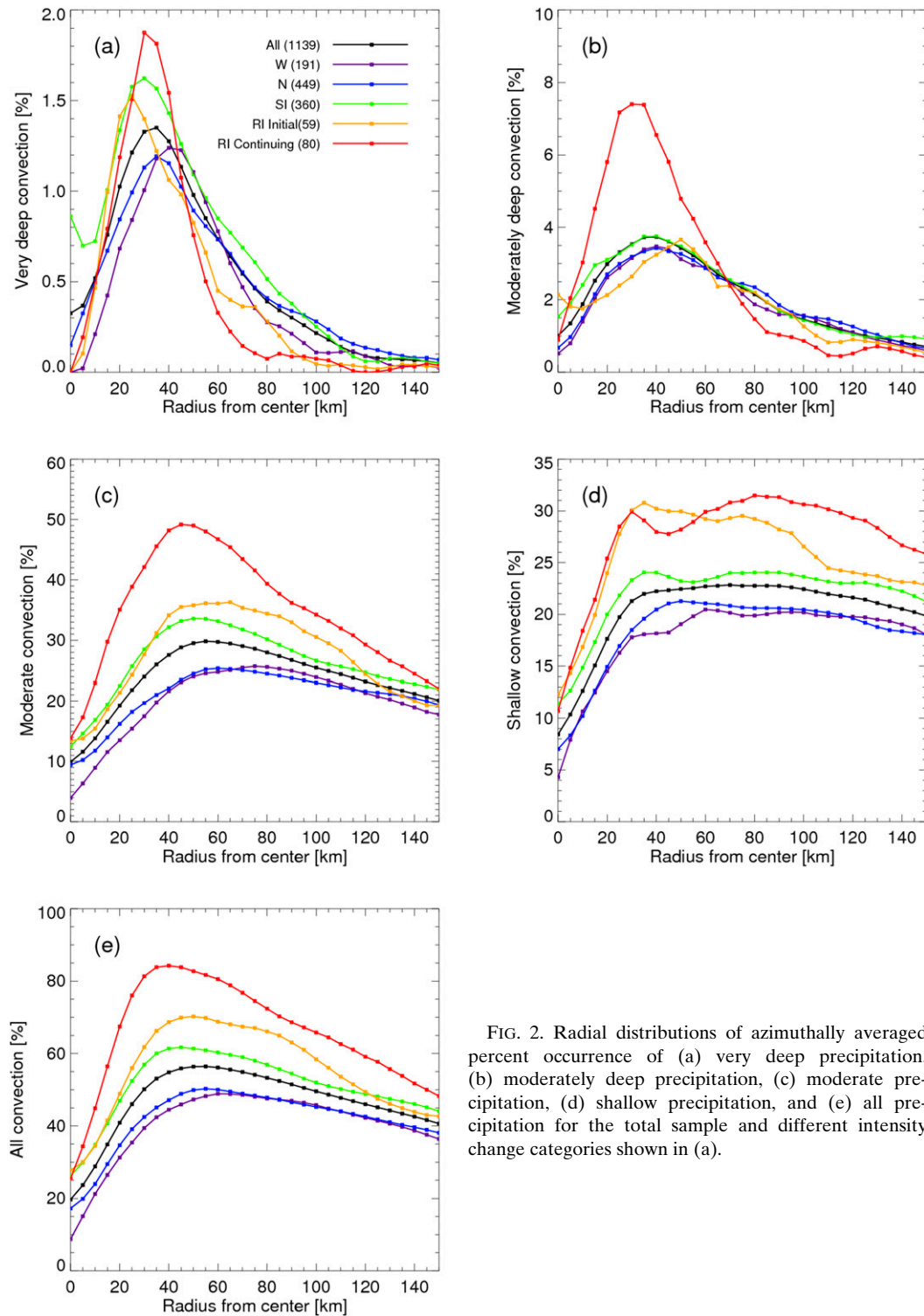


FIG. 2. Radial distributions of azimuthally averaged percent occurrence of (a) very deep precipitation, (b) moderately deep precipitation, (c) moderate precipitation, (d) shallow precipitation, and (e) all precipitation for the total sample and different intensity change categories shown in (a).

precipitation for all samples and different intensity change categories. The azimuthally averaged percent occurrence of precipitation is shown from the storm center outward to 150 km, corresponding to the inner-core

and inner-rainbands region (there is very little difference among various intensity change categories beyond 150 km). We are particularly interested in the difference between SI and RI initial categories to see if the

TABLE 4. Composite-mean values of the percent occurrence of precipitation in each shear-relative quadrant, averaged within 100 km of the TC center. Asterisks in the RI, RI initial, and RI continuing rows represent the statistical significance between SI and RI, SI and RI initial, and RI initial and RI continuing storms, respectively, at the 90% (*), 95% (**), 99% (***), and 99.9% (****) confidence levels.

| Very deep precipitation | DR | UR | UL | DL | Total |
|-------------------------------|-----------|-----------|-----------|---------|-----------|
| W | 0.25 | 0.17 | 0.80 | 1.13 | 0.60 |
| N | 0.40 | 0.13 | 0.64 | 1.41 | 0.65 |
| SI | 0.37 | 0.27 | 1.06 | 1.60 | 0.82 |
| RI | 0.37 | 0.11 | 0.79 | 0.87* | 0.53** |
| RI initial | 0.28 | 0.07 | 0.73 | 1.23 | 0.56** |
| RI continuing | 0.45 | 0.14 | 0.83 | 0.61 | 0.51 |
| All | 0.36 | 0.18 | 0.82 | 1.36 | 0.68 |
| Moderately deep precipitation | DR | UR | UL | DL | Total |
| W | 1.81 | 1.04 | 2.38 | 4.33 | 2.42 |
| N | 1.92 | 1.17 | 2.58 | 4.53 | 2.56 |
| SI | 2.03 | 1.28 | 2.99 | 4.37 | 2.65 |
| RI | 2.24 | 1.75** | 4.03** | 3.67 | 2.91 |
| RI initial | 1.58 | 1.12 | 4.11 | 3.25 | 2.47 |
| RI continuing | 2.79 | 2.29** | 3.98 | 3.98 | 3.27*** |
| All | 1.98 | 1.26 | 2.85 | 4.34 | 2.61 |
| Moderate precipitation | DR | UR | UL | DL | Total |
| W | 26.38 | 13.23 | 16.71 | 35.20 | 23.11 |
| N | 24.54 | 14.37 | 20.01 | 33.77 | 23.16 |
| SI | 31.29 | 20.89 | 25.18 | 42.72 | 30.00 |
| RI | 34.96 | 28.14**** | 39.65**** | 48.19** | 37.60**** |
| RI initial | 31.55 | 24.09 | 34.43** | 42.59 | 32.84 |
| RI continuing | 37.78 | 31.67** | 43.77* | 52.42** | 41.46*** |
| All | 28.28 | 17.99 | 23.40 | 38.51 | 27.06 |
| Shallow precipitation | DR | UR | UL | DL | Total |
| W | 19.37 | 13.21 | 18.74 | 24.53 | 19.09 |
| N | 21.07 | 14.04 | 20.25 | 24.64 | 20.00 |
| SI | 24.03 | 19.82 | 23.81 | 25.56 | 23.30 |
| RI | 31.38**** | 27.62**** | 27.99* | 29.72** | 29.15**** |
| RI initial | 30.71*** | 25.98*** | 27.51 | 30.55** | 28.60*** |
| RI continuing | 31.94 | 29.06 | 28.38 | 29.09 | 29.59 |
| All | 22.96 | 17.46 | 22.02 | 25.51 | 21.99 |

precipitation distributions can help forecasters distinguish the onset of RI from SI cases. The differences among SI, RI initial, and RI continuing cases are also important because the RI continuing category not only represents the middle of an RI event but also is useful for predicting the continuation of RI in the following 24 h.

It is quite rare for 20-dBZ reflectivity to reach the 14-km level, as the maximum percent occurrence is less than 2% (Fig. 2a). Overall, intensifying storms (including RI and SI) have higher peak values of percent occurrence of very deep precipitation than non-intensifying storms, which is consistent with the statistical study using airborne radar data in Rogers et al. (2013). RI continuing storms have the highest peak, followed by SI and RI initial storms. However, it is greater only in the 25–40-km range from the TC center. The frequencies of very deep precipitation for RI (both initial and continuing) storms drop below the other categories beyond

60 km. RI initial storms have a slightly lower percent occurrence of very deep precipitation than SI storms at all radial distances shown in Fig. 2a. Averaged within the innermost 100 km of the TC center, SI storms have the greatest percent occurrence of very deep precipitation (0.83%; Table 4), followed by N (0.65%), RI continuing (0.6%), W (0.56%), and RI initial (0.5%) storms. A Student's *t* test shows that SI storms have significantly more very deep precipitation than RI initial storms at the 95% confidence level.

Within 70 km from the storm center, RI continuing storms have a much higher frequency of moderately deep precipitation than storms in all other intensity change categories (Fig. 2b). The peak of the RI continuing curve (about 7.5%) is about double the rest of the categories. But similar to the very deep precipitation, the frequency of moderately deep precipitation also drops below the other categories beyond

70 km. Averaged within 100 km of the TC center, the mean percent occurrence of moderately deep precipitation for RI continuing storms is about 1.3% higher than that of RI initial cases. The difference is significant at the 99% confidence level. The percent occurrences of moderately deep precipitation for RI initial, SI, N, and W storms are very similar to each other (Fig. 2b; Table 4).

Figure 2c shows that RI continuing storms have the highest percent occurrence of moderate precipitation at all radial distances among all intensity change categories. The peak value is about 50%, appearing at the 40-km radius from the storm center. The mean percent occurrence within 100 km from the storm center for RI continuing storms is about 9% higher than that for RI initial storms, and the difference is significant at the 99% confidence level (Table 4). RI initial storms have a slightly higher percent occurrence of moderate precipitation than SI storms in the radial range of 40–120 km, while SI storms have a higher percent occurrence than N and W storms at all radial distances.

A pronounced difference between RI initial and SI storms is seen in Fig. 2d. The percent occurrences of shallow precipitation for both RI initial and RI continuing cases are similar, which are much higher than that of SI in all radial distances from the TC center. The peaks of the RI initial and RI continuing curves reach above 30%, which is about 7%–12% higher than those of the SI, N, and W curves. Table 4 shows that the difference of the mean inner-100-km percent occurrence of shallow precipitation between RI initial and SI storms is about 5% and is significant at the 99% confidence level. This implies that increased and widespread shallow precipitation may be the first sign of RI and may be used to distinguish RI onset from SI. Moderate precipitation also increases slightly (Fig. 2c) from the SI to RI initial category, but moderately deep and very deep precipitation do not increase until the later stage of RI (i.e., the RI continuing category; Figs. 2a,b) and therefore are a symptom instead of an indicator of the onset of RI.

Figure 2e presents the radial distribution of the percent occurrence of total precipitation (the sum of four types of precipitation), which is very similar to the rainfall frequency (percent occurrence of near-surface reflectivity exceeding 20 dBZ) shown in ZJ14's Fig. 5a. Significant differences in the frequency of total precipitation are found between SI, RI initial, and RI continuing cases. Based on airborne Doppler observations, Rogers et al. (2013) found that intensifying TCs have a higher azimuthal coverage of precipitation than steady-state TCs. They further argued that this difference may be due to the difference in the magnitude of vertical wind shear. However, in this study, the environmental

conditions (including vertical wind shear and the difference of shear direction and storm motion direction; see Table 3) are very similar between SI and RI initial cases. Therefore, the higher azimuthally averaged percent occurrence of total precipitation at the onset of RI may be due to internal factors. Comparing Figs. 2a–d with Fig. 2e, it is found that the difference of the occurrences of total precipitation between RI continuing and RI initial storms is mainly contributed by the difference in moderate and moderately deep precipitation, while the difference between RI initial and SI storms mainly comes from shallow and moderate precipitation. This implies that the increased amount of shallow–moderate precipitation may be used to predict the onset of RI, while the increased amount of moderate to moderately deep precipitation may be used to predict the continuation of RI in the next 24 h.

2) COMPOSITE IMAGES

The corresponding shear-relative distributions of percent occurrence of four types of precipitation are presented in Figs. 3–6, with the storm center in the middle and vertical wind shear pointing upward along the +y axis. According to the direction of the vertical wind shear vector, the upper-left, upper-right, lower-left, and lower-right quadrants are referred to as downshear left (DL), downshear right (DR), upshear left (UL), and upshear right (UR), respectively (Chen et al. 2006; ZJ14). Here, we focus only on the region within 100 km from the center. The 25-, 50-, 75-, and 100-km radii are shown as dotted rings in each panel. The quadrant-mean values of the percent occurrence of various kinds of precipitation, which are averaged in the innermost 100 km of the TC center, are shown in Table 4.

Figure 3 shows the composite shear-relative distribution of the frequency of very deep precipitation for W, N, SI, RI initial, and RI continuing storms. Previous studies have shown that the downshear-left quadrant is favored for the greatest rainfall frequency (ZJ14) and highest rain rates (Chen et al. 2006). The distributions of the very deep precipitation frequency for W, N, SI, and RI initial storms have a similar pattern as the rainfall distribution shown in Chen et al. (2006) and ZJ14, with the downshear-left quadrant containing significantly more very deep precipitation than any other quadrant (Figs. 3a–c,e; Table 4). In Fig. 3f for RI continuing storms, the maximum frequency of very deep precipitation shifts more toward the upshear-left quadrant with a secondary maximum located in the downshear-right quadrant. The modeling study of Hurricane Wilma (2005) by Zhang and Chen (2012) showed that convective bursts occurred mostly in the upshear quadrant when the storm underwent RI. The largest area of >1%

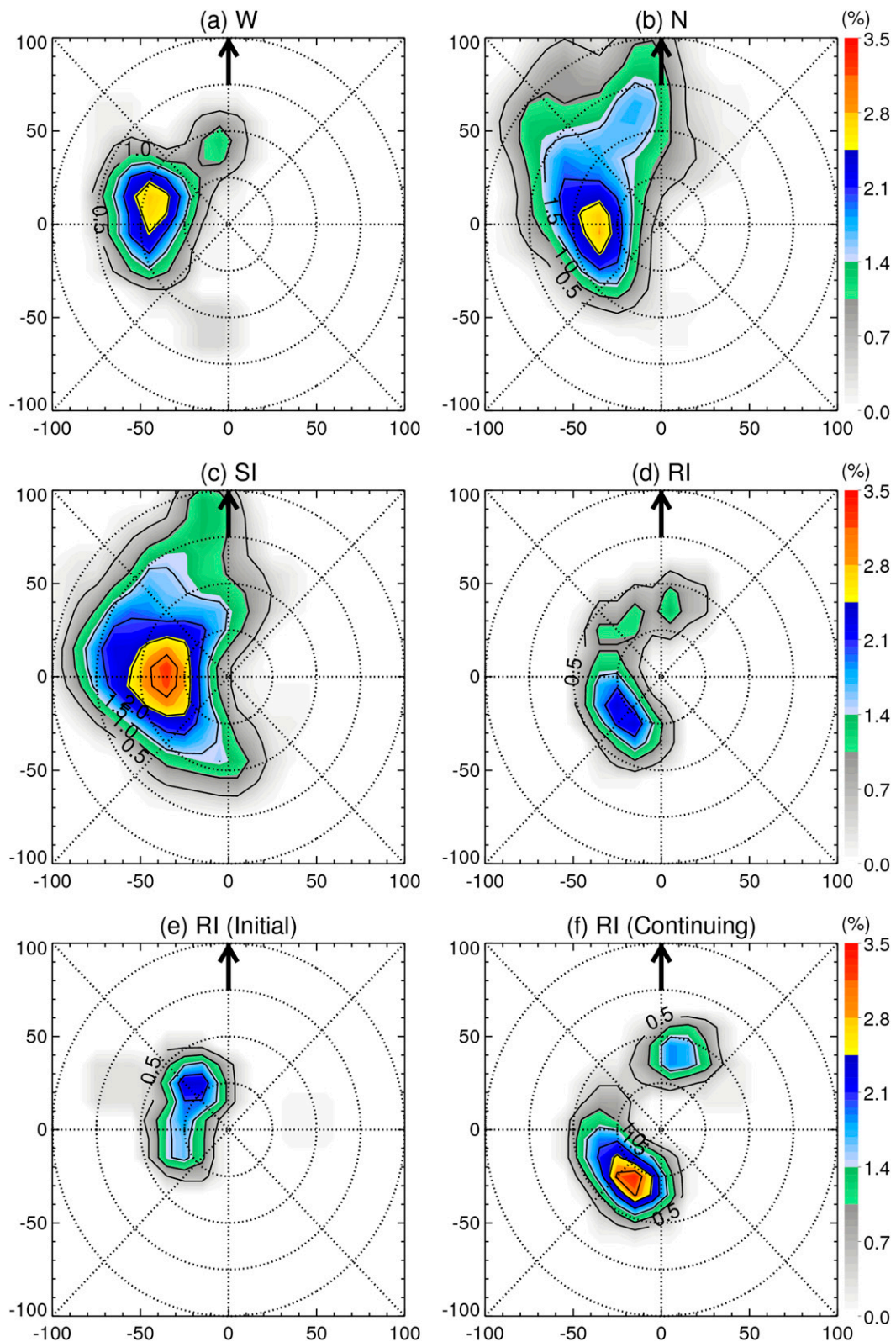


FIG. 3. Composite shear-relative distribution of the percent occurrence of very deep precipitation for (a) W, (b) N, (c) SI, (d) RI, (e) RI initial, and (f) RI continuing. The black arrow represents the orientation of the vertical wind shear vector. The 25-, 50-, 75-, and 100-km radii are shown as dotted rings.

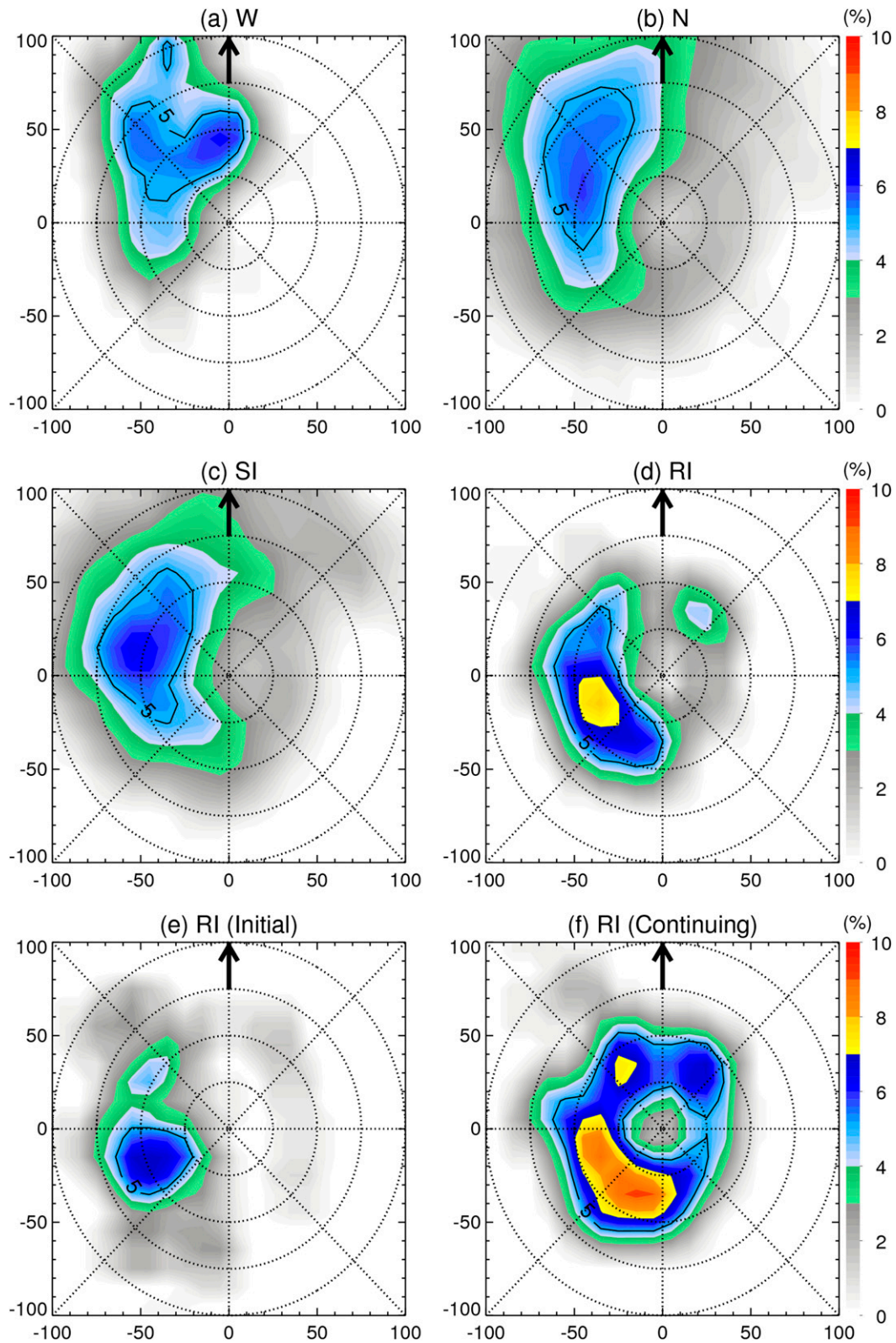


FIG. 4. As in Fig. 3, but for moderately deep precipitation.

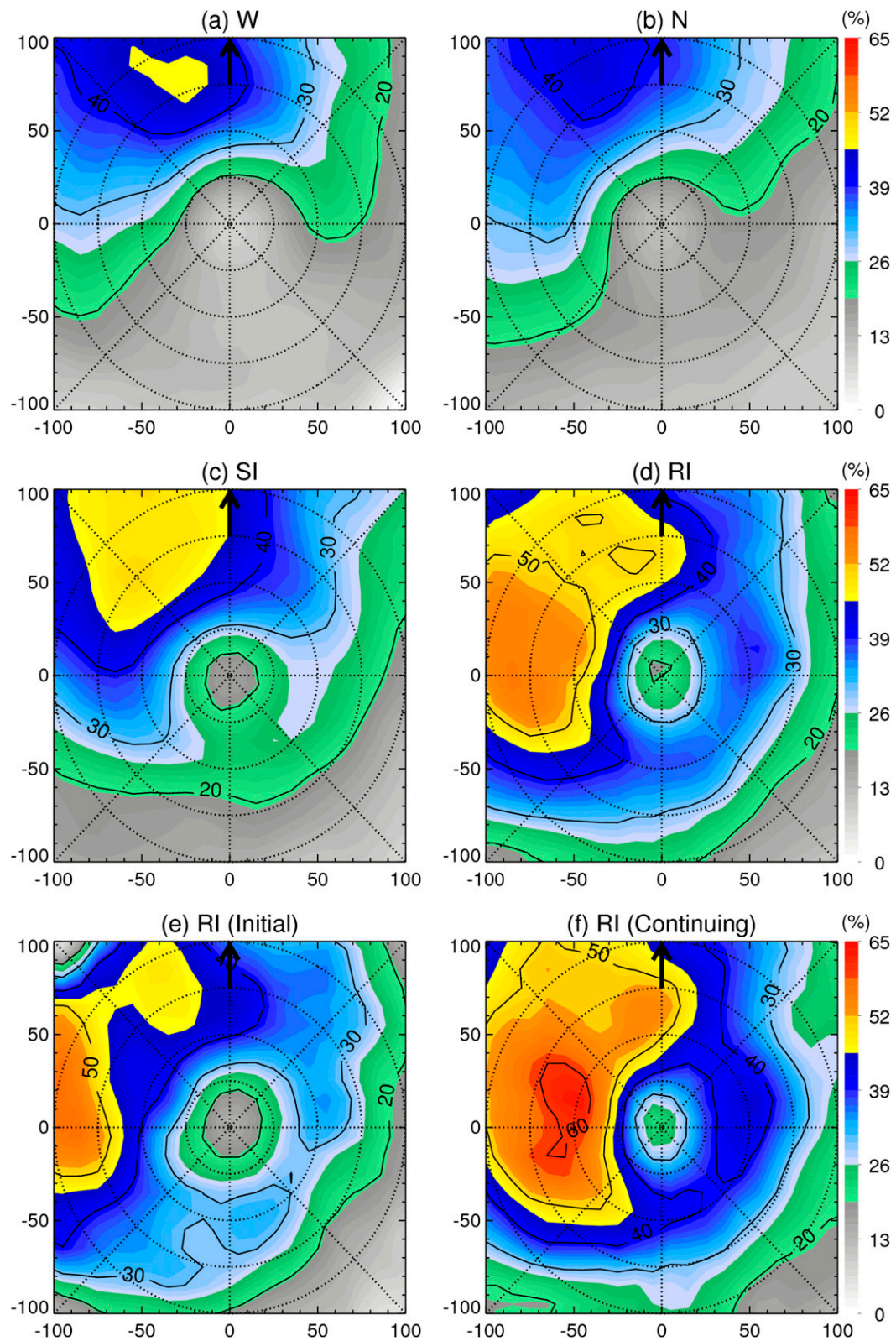


FIG. 5. As in Fig. 3, but for moderate precipitation.

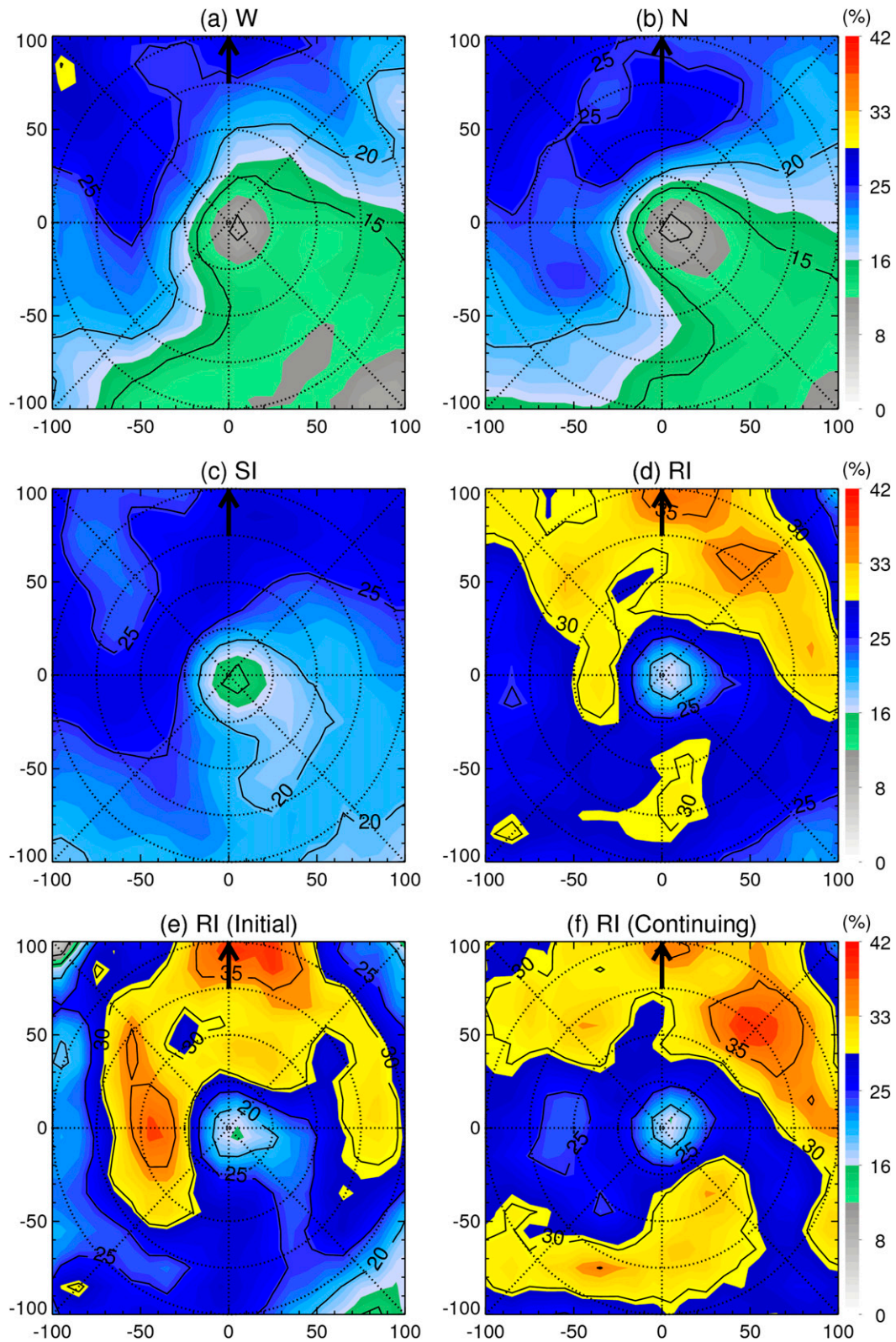


FIG. 6. As in Fig. 3, but for shallow precipitation.

occurrence of very deep precipitation is observed in SI storms (Fig. 3c), followed by N (Fig. 3b) and W (Fig. 3a) storms. Very deep precipitation is less widespread in RI continuing (Fig. 3f) and RI initial (Fig. 3e) storms. However, a major difference is observed in both RI continuing and initial cases, as the occurrences of very deep precipitation are almost entirely concentrated within the innermost 50 km, likely near or within the RMW. As estimated by ZJ14, in the TRMM PR dataset used in this study, the mean RMW is 49 km for SI and 38 km for the combined RI (initial and continuing) storms, which compares favorably with RMW values of 43 km for intensifying and 53 km for steady-state TCs in Rogers et al. (2013).

The percent occurrence of moderately deep precipitation in Fig. 4 indicates a similar pattern for weakening, neutral, and slowly intensifying storms (Figs. 4a–c), with the downshear-left quadrant containing significantly greater moderately deep precipitation than any other shear-relative quadrant. A remarkably different distribution is observed for RI continuing (Fig. 4f) and RI initial (Fig. 4e) storms, with the maximum frequency of moderately deep precipitation appearing in the upshear-left quadrant and located closer to the center (at 25–50 km for RI continuing storms and 25–75 km for RI initial storms). Figures 4c,e illustrate a pronounced difference between SI and RI initial cases in the upshear-left quadrant where RI initial storms have a much greater percent occurrence of moderately deep precipitation than SI storms. The opposite is true for any other shear-relative quadrant (Table 4). RI continuing storms (Fig. 4f) have a much more symmetric distribution compared with other intensity change categories. An almost closed ring of >5% occurrence in the innermost 50 km is found for RI continuing cases, with the maximum values located upshear left peaking around 10%.

Deep convection near or within the RMW has been linked to vortex strengthening in many studies (e.g., Vigh and Schubert 2009; Reasor et al. 2009; Molinari and Vollaro 2010; Rogers 2010; Nguyen and Molinari 2012; Rogers et al. 2013). However, Figs. 3–4 indicate that there is no more moderately deep–very deep precipitation–convection in RI initial storms than in W and N storms. This suggests that rapid intensification is likely triggered by other mechanisms and that the appearance of more deep convection in the middle of RI is more likely a response or positive feedback to changes in the vortex that occur earlier in the SI period to the beginning of the RI period.

For moderate precipitation, Fig. 5 shows that the downshear-left quadrant is favored in all categories. A similar pattern is observed for weakening and neutral

storms, and it is more asymmetric than that of SI and RI storms. For W and N storms (Figs. 5a,b), the maximum frequency of moderate precipitation is 40%–50% in the downshear-left quadrant, while less than 20% is upshear right. RI initial storms, with a more symmetric distribution, have more moderate precipitation than SI storms in all shear-relative quadrants (Fig. 5e). Moderate precipitation becomes more widespread and symmetric around the center as RI continues. An almost-closed ring of at least 40% occurrence around the center is found for RI continuing storms (Fig. 5f), while only 30% is found for RI initial storms (Fig. 5e). This indicates a significant increase of moderate precipitation during RI from the onset of RI in all quadrants.

Asymmetric distributions are also observed for both W and N storms in the percent occurrence of shallow precipitation (Figs. 6a,b), with a maximum of 25%–30% DL occurrence and less than 15% UR occurrence. SI storms (Fig. 6c) have a similar pattern to W and N storms but a higher frequency of shallow precipitation in the UR quadrant. Shallow precipitation is much more widespread for storms at the onset of RI, as a much higher percent occurrence is found for RI initial storms than SI storms in all shear-relative quadrants (Fig. 6e; Table 4). For RI initial storms, a ring of at least 25% occurrence of shallow precipitation is almost completely wrapping around the center, peaking at about 38%. As RI continues, the shallow precipitation does not increase as much as other types of precipitation, but the shear-relative distribution becomes more symmetric (Fig. 6f). Overall, Figs. 5–6 suggest that more widespread and more symmetric shallow–moderate precipitation is an indicator of either the onset, or the continuation, of RI.

From Figs. 3–6, we can see that the downshear-left quadrant is favored for all types of precipitation for W, N, and SI storms, consistent with results found by many previous studies for TCs in general (Corbosiero and Molinari 2002, 2003; Chen et al. 2006; Cecil 2007; Hence and Houze 2012). However, the shear-relative distributions for RI storms are remarkably different. For both RI initial and continuing storms (Figs. 6e,f), shallow precipitation peaks in the downshear-right quadrant, which is the quadrant where the triggering of convective updrafts begins, as indicated by previous studies (Black et al. 2002; Hence and Houze 2011, 2012). As precipitation becomes deeper, the location of peak precipitation rotates cyclonically for RI storms. Moderate precipitation peaks in the downshear-left quadrant, similar to all other intensity change categories (Fig. 5). From the composite analysis of airborne Doppler data, Reasor et al. (2013) also confirmed that the shear-relative TC asymmetry is featured by downshear-right

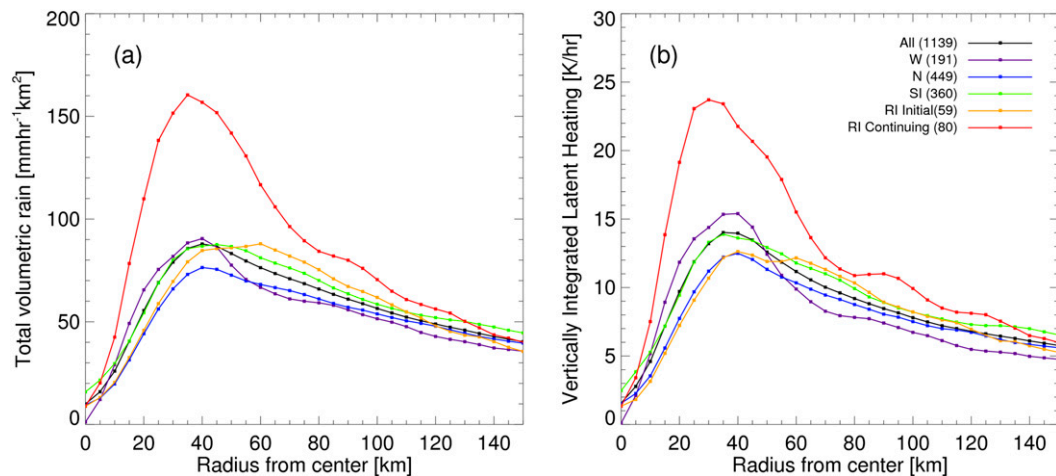


FIG. 7. Radial distributions of azimuthally averaged (a) total volumetric rain and (b) total vertically integrated latent heating for the total sample and different intensity change categories shown in (b).

convective initiation and a downshear-left precipitation maximum. Moderately deep precipitation peaks at the upshear-left quadrant (Figs. 4e,f). Very deep precipitation has double peaks in RI continuing storms (Fig. 3f), with the primary peak in the upshear-left quadrant and the secondary peak in the downshear-right quadrant. For RI initial storms (Fig. 3e), very deep precipitation peaks in the downshear-left quadrant, similar to W, N, and SI storms. The cyclonic rotation of peaks from shallow to deep precipitation follows the wind direction around the TC center. One may argue that this rotation simply reflects the trajectory of air parcels as they ascend in cyclonic flow, as in Black et al. (2002). However, from Figs. 3–6, this rotating feature is seen only in RI storms, not in W, N, and SI storms. Therefore, we argue that this may be an indicator of the vortex rapidly strengthening. As a storm rapidly intensifies, it may be more resilient to shear, causing the fall-out of ice particles generated upstream to be increasingly prevalent azimuthally downwind (Hence and Houze 2012).

b. Total volumetric rain

The radial distributions of total volumetric rain and total latent heating in Fig. 7 illustrate similar patterns for W, N, SI, and RI initial storms, while RI continuing storms have remarkably higher azimuthally averaged total rainfall and latent heating than other intensity change categories. Similarly, previous studies (e.g., Jiang and Ramirez 2013; Kieper and Jiang 2012) have shown that RI storms have widespread precipitation with high total volumetric rain in the inner-core region. However, this study further indicates that it is RI continuing storms that account for the pronounced difference of total volumetric rain and latent heating between

SI and RI storms, as the curves for RI initial and SI storms are very similar. Table 5 also shows that in the innermost 100 km of the TC center, the mean differences between SI and RI initial storms in total volumetric rain and latent heating are not statistically significant. Without separating RI initial and continuing categories, Jiang and Ramirez (2013) concluded that large total raining area and total volumetric rain in the inner core are necessary conditions of RI. However, our results here indicate that this conclusion is valid only for the RI continuing category.

The composite shear-relative distributions of total volumetric rain for various intensity change categories are displayed in Fig. 8. Consistent with previous studies, the maximum total volumetric rain is downshear and to the left of the shear vector (e.g., Chen et al. 2006; Wingo and Cecil 2010). As shown in Figs. 8a–d, the maximum total volumetric rain occurs in the downshear-left quadrant in all intensity change categories except in the RI continuing category, in which the maximum is mainly upshear left. These distributions are similar to the mean rain rates in Figs. 16–18 of Wingo and Cecil (2010) and the averaged vertically integrated latent heat in Fig. 9 of ZJ14. Although the mean inner-100-km total volumetric rain is similar for SI and RI initial storms, a substantial difference is observed in the upshear-left quadrant. An almost-closed ring of $40 \text{ mm h}^{-1} \text{ km}^2$ total volumetric rain is found surrounding the storm center for RI initial storms, but only $20\text{--}30 \text{ mm h}^{-1} \text{ km}^2$ of total volumetric rain surrounds the storm center for SI storms. For RI continuing storms (Fig. 8f), the maximum total volumetric rain is located in the upshear-left quadrant between 25 and 50 km of the center and peaking at about $200 \text{ mm h}^{-1} \text{ km}^2$, with a ring of at least

TABLE 5. Mean values of total volumetric rain ($\text{mm h}^{-1} \text{km}^2$) and total vertically integrated latent heating (K h^{-1}) in each shear-relative quadrant within 100 km of the TC center. Asterisks in the RI, RI initial, and RI continuing rows represent the statistical significance between SI and RI, SI and RI initial, and RI initial and RI continuing storms, respectively, at the 90% (*), 95% (**), 99% (***), and 99.9% (****) confidence levels.

| Total volumetric rain | DR | UR | UL | DL | Total |
|--------------------------|-------|-----------|-----------|--------|------------|
| W | 47.00 | 18.19 | 45.63 | 118.03 | 65.65 |
| N | 47.88 | 20.75 | 46.27 | 109.76 | 62.31 |
| SI | 63.52 | 29.70 | 53.77 | 121.63 | 74.19 |
| RI | 71.84 | 52.15**** | 90.98**** | 117.57 | 92.37**** |
| RI initial | 61.49 | 35.54 | 73.68** | 108.57 | 73.96 |
| RI continuing | 79.47 | 64.40*** | 103.74** | 124.21 | 105.94**** |
| All | 55.60 | 26.98 | 53.99 | 115.85 | 70.29 |
| Vertically integrated LH | DR | UR | UL | DL | Total |
| W | 6.94 | 2.61 | 6.86 | 18.20 | 9.78 |
| N | 7.17 | 3.08 | 6.79 | 17.44 | 9.47 |
| SI | 9.75 | 4.19 | 8.08 | 19.33 | 11.10 |
| RI | 10.66 | 7.24**** | 12.63**** | 16.70 | 13.03** |
| RI initial | 8.95 | 4.50 | 10.64 | 15.52* | 10.34 |
| RI continuing | 11.92 | 9.27**** | 14.10 | 17.57 | 15.02**** |
| All | 8.37 | 3.86 | 7.92 | 18.08 | 10.47 |

$100 \text{ mm h}^{-1} \text{ km}^2$ extending completely around the center. The mean total volumetric rain (latent heating) within 100 km of the storm center in RI continuing storms is about $30 \text{ mm h}^{-1} \text{ km}^2$ ($4\text{--}5 \text{ K h}^{-1}$) higher than those in SI and RI initial storms (Table 5), similar to Fig. 7.

c. Contribution to total volumetric rain and total latent heating

To quantify the contribution of each type of precipitation to total volumetric rain, Table 6 shows the mean values of the percentage of total rainfall from four kinds of precipitation, which is averaged within 100 km of the TC center. It is found that moderate precipitation accounts for about 63% of total volumetric rain, while the other three kinds of precipitation together account for only 37%. Overall, the percentage of total rainfall from moderate precipitation is about 11, 5, and 3 times greater than that from very deep precipitation, moderately deep precipitation, and shallow precipitation, respectively (Tables 6 and 7). Similar results are found for the contribution to total latent heating. Note that the total percent occurrence of all four types of precipitation within the 100-km radius is about 52% (Table 4). Therefore, the relative pixel-based contribution to total precipitation of very deep precipitation, moderately deep precipitation, moderate precipitation, and shallow precipitation is about 1%, 5%, 52%, and 42%, respectively (Table 7). Comparing these numbers with the percentage contributions to total volumetric rain and total latent heating shown in Table 7, we can see that both very deep precipitation and moderately deep precipitation have a disproportionately higher contribution to total volumetric rain and total latent heating.

In the innermost 100 km, about 1% (5%) of total convective pixels is very deep precipitation (moderately deep precipitation), but these pixels contribute about 6% and 9% (12% and 15%) to the total rainfall and total latent heating, respectively. However, for RI versus non-RI categories, Table 7 indicates that the percentage of total volumetric rain (total latent heating) contributed by moderately to very deep precipitation is smaller in RI storms (including RI initial and RI continuing) than in non-RI storms (including W, N, and SI), while the opposite is true for shallow–moderate precipitation. This suggests that the contribution of shallow–moderate precipitation to the total rainfall and latent heating is more important to the initiation and maintenance of RI.

The corresponding composite shear-relative distributions of the percentage of the total volumetric rain from four kinds of precipitation are shown in Figs. 9–12. The distributions for the total latent heating are quite similar and thus not shown here, as mentioned in the introduction. Figure 9 illustrates that the maximum contribution of very deep precipitation to total volumetric rain is located in the upshear-left quadrant for all intensity change categories except for the RI initial category, in which the maximum is located downshear-left. RI continuing storms (Fig. 9f) have a second maximum located in the downshear-right quadrant. Averaged within the innermost 100 km of the TC center, RI continuing storms have the lowest percentage of total volumetric rain from very deep precipitation. The difference between SI and RI storms in the convective contribution to total rainfall is about 3.5%, which is significant at the 95% confidence level (Table 6).

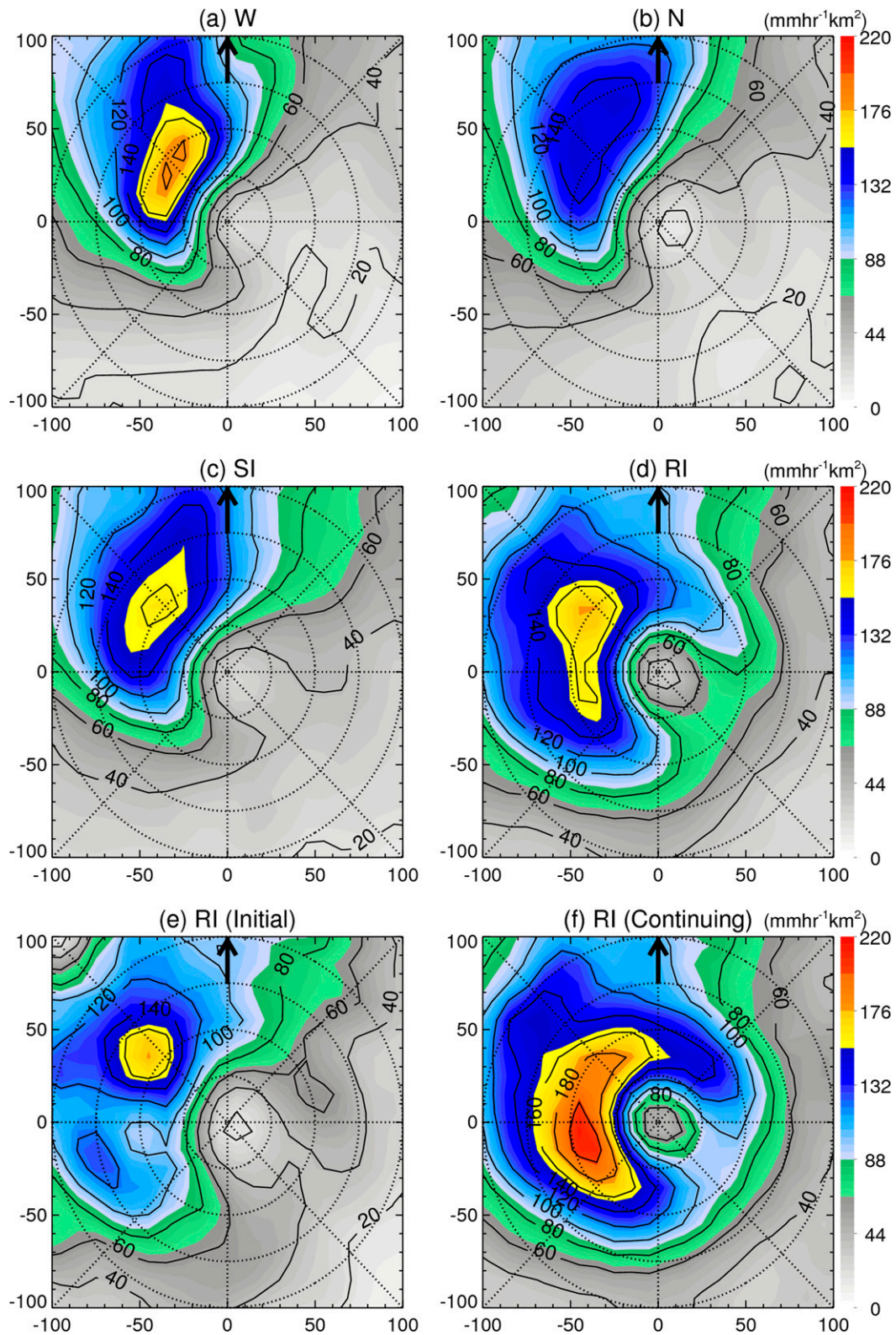


FIG. 8. Composite shear-relative distribution of the averaged total volumetric rain for (a) W, (b) N, (c) SI, (d) RI, (e) RI initial, and (f) RI continuing. The black arrow represents the orientation of the vertical wind shear vector. The 25-, 50-, 75-, and 100-km radii are shown as dotted rings.

TABLE 6. Composite-mean values of the convective contribution to total volumetric rain in each shear-relative quadrant, averaged within 100 km of the TC center. Asterisks in the RI, RI initial, and RI continuing rows represent the statistical significance between SI and RI, SI and RI initial, and RI initial and RI continuing storms, respectively, at the 90% (*), 95% (**), 99% (***), and 99.9% (****) confidence levels.

| Very deep precipitation | DR | UR | UL | DL | Total |
|-------------------------------|--------|----------|----------|---------|----------|
| W | 1.76 | 4.08 | 7.71 | 4.57 | 4.59 |
| N | 3.50 | 1.87 | 8.21 | 7.70 | 6.38 |
| SI | 2.71 | 4.29 | 9.34 | 8.53 | 6.85 |
| RI | 3.18 | 0.66 | 4.03 | 3.88* | 3.28** |
| RI initial | 2.95 | 0.37** | 4.13 | 6.17 | 4.15 |
| RI continuing | 3.31 | 0.80 | 3.97 | 2.44 | 2.79 |
| All | 2.92 | 2.70 | 7.62 | 6.92 | 5.75 |
| Moderately deep precipitation | DR | UR | UL | DL | Total |
| W | 9.05 | 8.41 | 12.37 | 12.92 | 11.68 |
| N | 11.50 | 10.04 | 13.85 | 15.82 | 13.96 |
| SI | 10.26 | 7.81 | 12.94 | 14.54 | 12.46 |
| RI | 9.42 | 6.53* | 12.98 | 9.63 | 10.06 |
| RI initial | 7.66 | 4.29 | 16.07 | 8.69** | 9.90 |
| RI continuing | 10.40* | 7.62*** | 11.29 | 10.22 | 10.14 |
| All | 10.39 | 8.25 | 13.18 | 14.11 | 12.48 |
| Moderate precipitation | DR | UR | UL | DL | Total |
| W | 68.83 | 58.67 | 54.22 | 64.77 | 63.03 |
| N | 64.53 | 59.97 | 53.56 | 61.40 | 60.34 |
| SI | 68.62 | 63.06 | 57.28 | 64.10 | 63.69 |
| RI | 64.37 | 68.27 | 67.23 | 70.37** | 67.94*** |
| RI initial | 63.20 | 63.50* | 62.38** | 66.46 | 64.30* |
| RI continuing | 65.02 | 70.60* | 69.89 | 72.82 | 70.01 |
| All | 66.57 | 62.83 | 57.63 | 64.00 | 63.08 |
| Shallow precipitation | DR | UR | UL | DL | Total |
| W | 20.31 | 28.67 | 25.63 | 17.73 | 20.69 |
| N | 20.41 | 27.98 | 24.31 | 15.06 | 19.32 |
| SI | 18.35 | 24.74 | 20.38 | 12.80 | 17.00 |
| RI | 22.98 | 24.46*** | 15.74 | 16.11 | 18.72** |
| RI initial | 26.12 | 31.70 | 17.37*** | 18.65 | 21.65 |
| RI continuing | 21.24* | 20.92*** | 14.84 | 14.52 | 17.06 |
| All | 20.06 | 26.10 | 21.52 | 14.95 | 18.68 |

Figure 10 displays the shear-relative distribution of the percentage of total volumetric rain from moderately deep precipitation. The maximum convective contribution is upshear-left for all intensity change categories except for the weakening storms (Fig. 10a), in which the maximum is downshear left. Overall, RI storms have higher contributions closer to the storm center. From Table 6, we can also see that when averaged for all quadrants, moderately deep precipitation accounts for similar percentages of total volumetric rain for RI initial, RI continuing, and SI, but some differences are seen in individual quadrants.

Within the innermost 100 km, moderate precipitation accounts for about 68% of total volumetric rain for all RI storms but only 60%–64% for neutral, weakening, and SI storms (Table 6). A pronounced difference (about 4%, significant at the 99% confidence level) is observed between SI and RI storms. The quadrant-mean

values of the contribution to total rainfall in Table 6 indicates that in the upshear-left quadrant, moderate precipitation accounts for approximately 62% to the total volumetric rain for RI initial storms, which is about 5% higher than SI storms (significant at the 95% confidence level). In the upshear-right quadrant, the contribution is 7% higher for RI continuing storms than RI initial storms (significant at the 90% confidence level). The corresponding shear-relative distribution in Fig. 11 illustrates that both RI initial (Fig. 11e) and RI continuing storms (Fig. 11f) have a much larger area with at least 70% total volumetric rain from moderate precipitation than other intensity change categories. A more symmetric pattern is seen for RI continuing storms (Fig. 11f).

Averaged within the innermost 100 km of the TC center, about 19% of the total volumetric rain is from shallow precipitation (Table 5). But it should be noted

TABLE 7. Composite-mean values of the percentage contribution of the four kinds of precipitation to total precipitation and total volumetric rain, averaged within 100 km of the TC center.

| Percent to total precipitation | W | N | SI | RI | RI initial | RI continuing | Total |
|---|-------|-------|-------|-------|------------|---------------|-------|
| Very deep precipitation | 1.32 | 1.40 | 1.44 | 0.75 | 0.86 | 0.68 | 1.30 |
| Moderately deep precipitation | 5.36 | 5.51 | 4.67 | 4.15 | 3.84 | 4.36 | 4.98 |
| Moderate precipitation | 51.11 | 49.96 | 52.84 | 53.57 | 50.94 | 55.41 | 51.70 |
| Shallow precipitation | 42.21 | 43.14 | 41.04 | 41.53 | 44.36 | 39.55 | 42.03 |
| Very deep + moderately deep precipitation | 6.68 | 6.91 | 6.11 | 4.9 | 4.7 | 5.04 | 6.28 |
| Moderate + shallow precipitation | 93.32 | 93.1 | 93.88 | 95.1 | 95.3 | 94.96 | 93.73 |
| Percent to total volumetric rain | W | N | SI | RI | RI initial | RI continuing | Total |
| Very deep precipitation | 4.59 | 6.38 | 6.85 | 3.28 | 4.15 | 2.79 | 5.75 |
| Moderately deep precipitation | 11.68 | 13.96 | 12.46 | 10.06 | 9.90 | 10.14 | 12.48 |
| Moderate precipitation | 63.03 | 60.34 | 63.69 | 67.94 | 64.30 | 70.01 | 63.08 |
| Shallow precipitation | 20.69 | 19.32 | 17.00 | 18.72 | 21.65 | 17.06 | 18.68 |
| Very deep + moderately deep precipitation | 16.27 | 20.34 | 19.31 | 13.34 | 14.05 | 12.93 | 18.23 |
| Moderate + shallow precipitation | 83.72 | 79.66 | 80.69 | 86.66 | 85.95 | 87.07 | 81.76 |
| Percent to total latent heat | W | N | SI | RI | RI initial | RI continuing | Total |
| Very deep precipitation | 7.21 | 9.47 | 10.71 | 4.90 | 6.32 | 4.09 | 8.83 |
| Moderately deep precipitation | 14.52 | 17.14 | 15.23 | 12.99 | 13.25 | 12.85 | 15.47 |
| Moderate precipitation | 63.21 | 60.10 | 62.10 | 68.14 | 65.07 | 69.89 | 62.46 |
| Shallow precipitation | 15.06 | 13.29 | 11.96 | 13.97 | 15.35 | 13.18 | 13.24 |
| Very deep + moderately deep precipitation | 21.73 | 26.61 | 25.94 | 17.89 | 19.57 | 16.94 | 24.3 |
| Moderate + shallow precipitation | 78.27 | 73.39 | 74.06 | 82.11 | 80.42 | 83.07 | 75.7 |

that the definition of shallow precipitation in this study does not involve any ice phase. Thus, the rain rate from shallow precipitation may be underestimated as a result of the TRMM PR 2A25 algorithm (Iguchi et al. 2000). Although the percent occurrence of shallow precipitation is much higher in RI storms than non-RI storms, shallow precipitation accounts for similar percentages to the total volumetric rain for RI and non-RI storms. This is mainly because of the higher contribution to the total volumetric rain from moderate precipitation for all RI storms. The corresponding composite shear-relative distribution in Fig. 12 illustrates that the upshear or upshear-right quadrants are favored in all intensity change categories in the contribution to the total rainfall. For weakening storms (Fig. 12a), a large area of 30% rainfall from shallow precipitation is observed within the innermost 25-km region.

4. Discussion

Consistent with previous satellite-based statistical studies (Jiang 2012; Kieper and Jiang 2012; Jiang and Ramirez 2013; ZJ14), results in this study suggest that widespread relatively symmetric shallow–moderate precipitation is more important in initiating and maintaining RI in the next 24 h than moderately to very deep convection. This seems to conflict with the observational case studies mentioned in the introduction (Reasor et al. 2009; Guimond et al. 2010; Molinari and Vollaro 2010;

Nguyen and Molinari 2012; Reasor and Eastin 2012), which emphasized the role of asymmetric very deep convection in RI. However, after careful scrutiny, it is found that in all of these observational case studies, the occurrence of very deep convection was observed within 24 h before an RI event ends. This is totally different from the definition of RI used in this study and previous satellite-based statistical studies mentioned above. As mentioned in section 2b, RI typically occurs as an event, which is defined as multiple, continuous, and overlapping 24-h periods in which the intensity increases in each period by 30 kt or more (Kieper and Jiang 2012). Each 24-h period within an RI event corresponds to one RI case as defined by Kaplan and DeMaria (2003). Based on a statistics using 1998–2013 global best-track data, the mean and median duration of all RI events is about 36 h with a minimum of 24 h [this is by the definition of Kaplan and DeMaria (2003)] and a maximum of 78 h. Figure 13 illustrates a schematic of a typical RI event, with the corresponding RI initial and RI continuing periods as defined in this study and an additional period called RI ending. The RI ending category includes the period during which an RI event will end within 24 h. Unlike RI initial and RI continuing categories, which require at least 24 h before an RI event ends, the RI ending category has no predictive power and may correspond to the weakening, neutral, or SI category as defined in this study. In the above-mentioned observational case studies, very deep

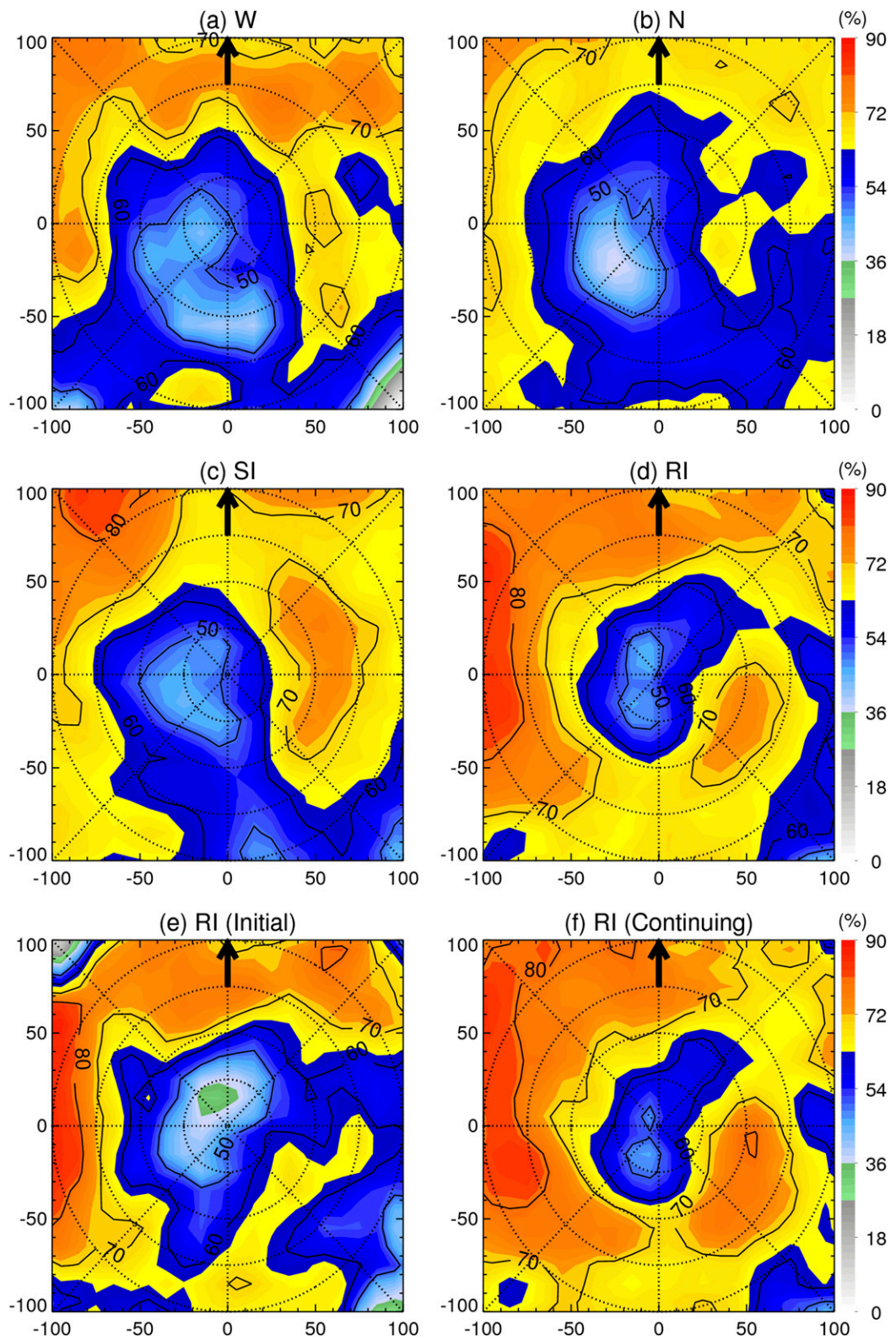


FIG. 11. As in Fig. 9, but for moderate precipitation.

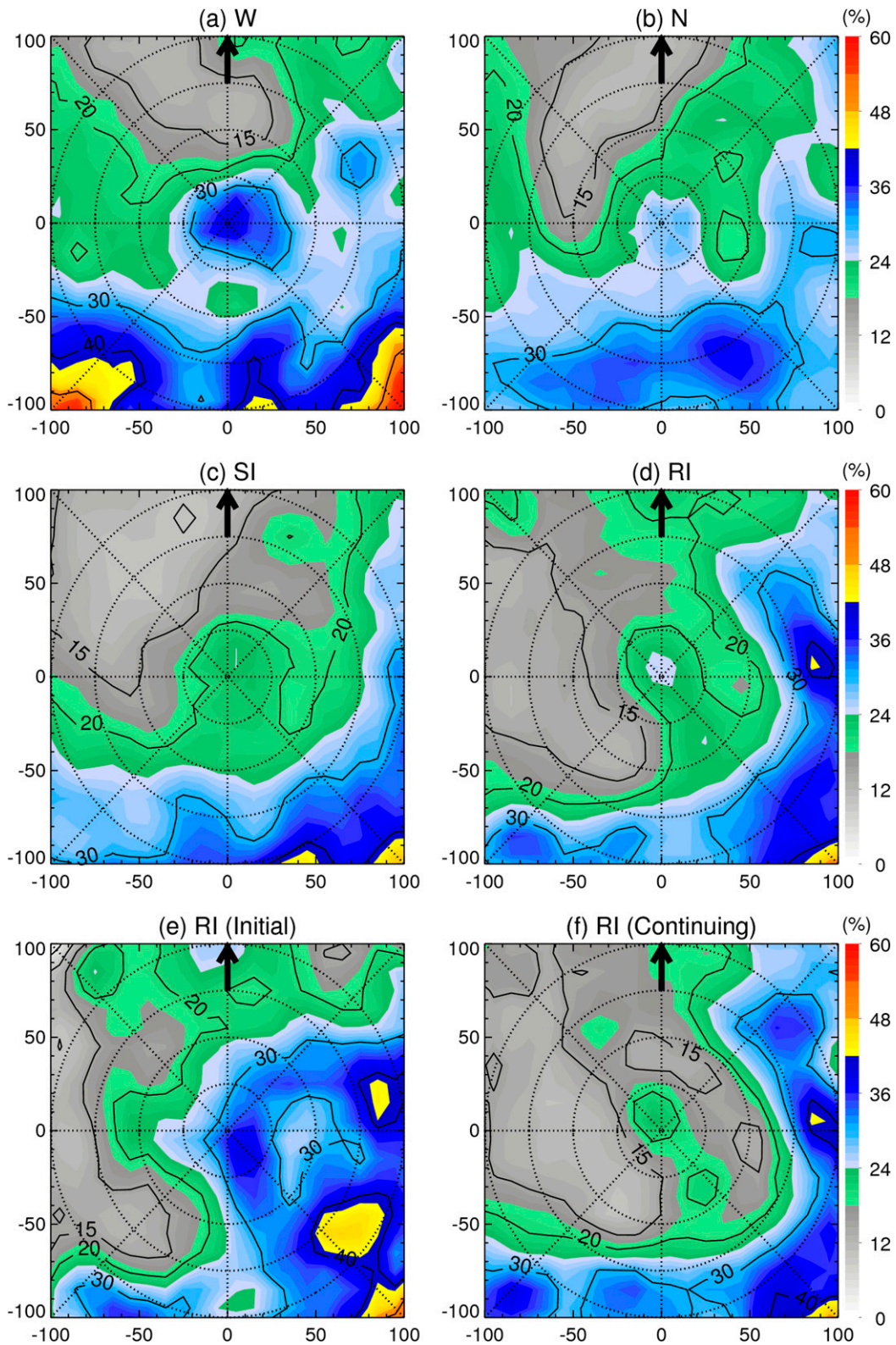


FIG. 12. As in Fig. 9, but for shallow precipitation.

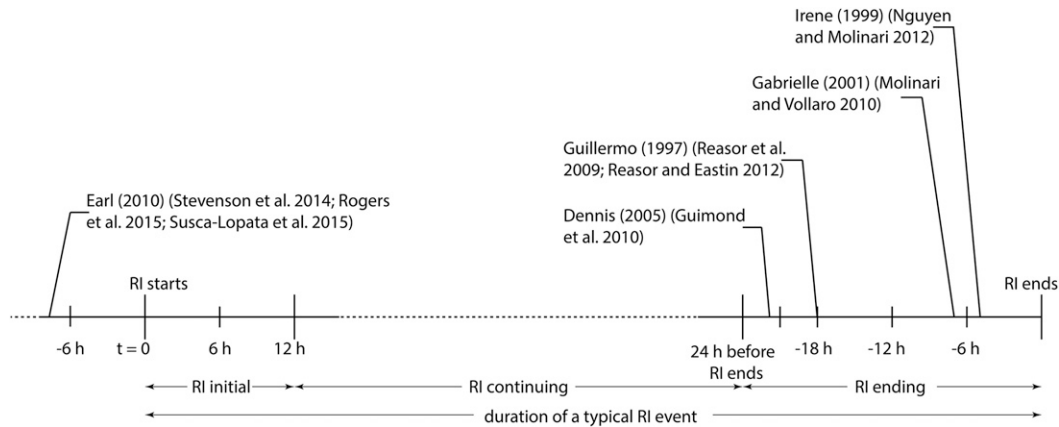


FIG. 13. Schematic of RI initial, RI continuing, and RI ending periods within a typical RI event. The relative time when the very deep convection was observed in each of the observational studies mentioned in section 4 is placed on the timeline in the RI ending period and before RI. Please see text for details.

convection that was claimed to play a role in RI was all in the RI ending period. As illustrated on the timeline in Fig. 13, deep convection observed in Hurricane Guillermo (1997) by aircraft during 1845 UTC 2 August–0012 UTC 3 August was only observed about 18 h before the RI event ended (Reasor et al. 2009; Reasor and Eastin 2012). Guimond et al. (2010) reported that the ER-2 aircraft observed a hot tower in Hurricane Dennis (2005), but it occurred around 22 h before the RI event ended. A hot tower occurred 5 h before the RI ended for Hurricane Irene (1999) in Nguyen and Molinari (2012). A vortical hot tower was observed 7 h before the RI event of Tropical Storm Gabrielle (2001) ended (Molinari and Vollaro 2010). There are several recent studies about Hurricane Earl (2010) (Stevenson et al. 2014; Rogers et al. 2015; Susca-Lopata et al. 2015) showing asymmetric deep convection around 6–9 h before the onset of RI (Fig. 13). At that time Earl was in the slowly intensifying stage. As seen in Fig. 3c of this study, very deep convection does increase in SI storms.

So the findings of these Earl studies are consistent with the current study.

Based on the findings of this study and above-mentioned observational case studies, Fig. 14 presents a hypothesized sequence of events providing some mechanisms to describe the importance of shallow–moderate precipitation, as opposed to deep–very deep convection, to RI. Before a storm undergoes RI, it is usually in the slowly intensifying or steady-state stage. At this time, isolated very deep convection is often observed (Fig. 3c; Stevenson et al. 2014; Rogers et al. 2015; Susca-Lopata et al. 2015), which is possibly due to high wind shear (Molinari and Vollaro 2010; Susca-Lopata et al. 2015), vortex misalignment (Stevenson et al. 2014; Rogers et al. 2015; Susca-Lopata et al. 2015), or dry environment (Stevenson et al. 2014). At the onset of RI (RI initial stage), increased shallow and moderate precipitation is seen, especially in the upshear quadrants (Figs. 5e and 6e; Susca-Lopata et al. 2015), inducing moistening and preconditioning for deep convection (Johnson et al.

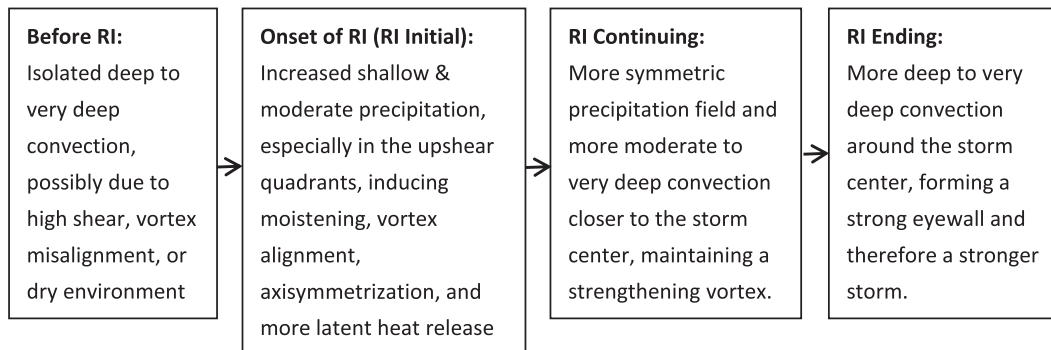


FIG. 14. A hypothesized sequence of events providing some mechanisms before and during RI that describes the importance of shallow–moderate precipitation as opposed to deep–very deep convection. Please refer to Fig. 13 for the definition of RI initial, RI continuing, and RI ending.

1999), vortex alignment (Chen and Gopalakrishnan 2015), axisymmetrization (Kieper and Jiang 2012; Suslopatina et al. 2015), and more latent heat release. As RI continues, increased moderate to very deep precipitation is observed, producing much higher total volumetric rain and latent heating release (Figs. 4f, 5f, and 6f; Table 5). The factors of very deep convection closer to the storm center (Figs. 3f and 4f) and the axisymmetrization of the precipitation field (Fig. 8f) help maintain the vortex's rapid strengthening for more than 24 h following. At the RI ending stage (<24 h before RI ends), there is a higher chance of having more deep–very deep convection around the storm center (Reasor et al. 2009; Guimond et al. 2010; Molinari and Vollaro 2010; Nguyen and Molinari 2012; Reasor and Eastin 2012), which helps form a strong eyewall and lead to a stronger storm.

Using aircraft Doppler radar data, Rogers et al. (2013) found that intensifying storms have a larger percentage of convective bursts within 1–2 times of the RMW than steady-state storms. Their definition of intensifying storms contains RI and part of the SI categories in this study. From Figs. 2–3 in this study, we can see that very deep precipitation (similar to their convective burst definition) does have higher peaks, which are located closer to the center in RI and SI storms than in neutral and weakening storms (similar to their steady-state definition). However, after integrating with the 100-km radius [about two RMW; see section 3a(ii) for details], we found that both the frequency of very deep precipitation and its contribution to total volumetric rain and total latent heating are much less in RI storms than those in neutral and weakening storms (Table 7). More interestingly, Table 7 does show that SI storms have a higher frequency and larger percent contributions to total volumetric rain and total latent heating from very deep precipitation than RI, neutral, and weakening storms. This suggests that 1) Rogers et al.'s (2013) intensifying storms might contain more SI storms than RI storms, which is possibly true owing to the limitation of aircraft data, and 2) very deep convection seems to play a more important role in slowly intensifying storms than in RI storms.

Another important point from the introduction is to examine the percent occurrence of total precipitation (including shallow, moderate, moderately deep, and very deep precipitation as defined in section 2c) in order to test if the cyan and pink color ring in the NRL 37-GHz color product found by Kieper and Jiang (2012) is precipitative. To do this, it was necessary to degrade the PR pixel size into TMI 37-GHz equivalent footprint size. The shear-relative distributions of the percent occurrence of total precipitation degraded to the 37-GHz

footprint size are shown in Fig. 15. As expected, the downshear-left quadrant is favored for all TC intensity change categories (e.g., Corbosiero and Molinari 2002; Chen et al. 2006). The precipitative/convective frequency, as well as the degree of symmetry, increases in order from weakening/neutral, SI, RI initial, to RI continuing storms. A ring of about 90% occurrence of all precipitation is observed for RI continuing storms (Fig. 15f), which is analogous to the cyan and pink ring feature recognized in Kieper and Jiang (2012) for RI storms. In this study, at least 20-dBZ PR reflectivity at different levels is required for all four types of precipitation. Therefore, all the precipitation defined in this study contains precipitation-sized particles.

One may ask how many cases that make up the RI composites in Figs. 3–6 and 15 have a 37-GHz cyan and pink ring. As shown in Table 2, 42 (70) out of the 59 (80) RI initial (continuing) cases have a 37-GHz ring within the TMI swath. Therefore, 112 out of 139 total RI cases (about 80%) have the ring feature for the 14-yr global TC data from the TRMM PR. The percentage is similar to what Kieper and Jiang (2012) found for Atlantic TCs during 2002–07. To carefully compare the 37-GHz cyan and pink ring with the PR reflectivity field, a subset of overpasses is further selected for cases with the cyan and pink ring directly covered by the PR swath. As shown in Table 2's last column, a total of 83 cases meet this criterion, including 30 RI initial and 53 RI continuing overpasses. Two examples of such overpasses are shown in Figs. 16 and 17 for an RI continuing case and an RI initial case, respectively. The Atlantic Hurricane Danielle (2004) case shows a 37-GHz cyan ring in the inner edge around the storm center with a pink arc on top of the eastern half of the cyan ring (Fig. 16a), while the northwestern Pacific Typhoon Marenti (2004) overpass also shows a 37-GHz cyan and pink ring, with the pink arc on the southwest side of the center (Fig. 17a). A complete 20-dBZ radar reflectivity ring is seen in both the Danielle and Marenti overpasses (Figs. 16b and 17b), resembling the 37-GHz cyan and pink ring. Harnos and Nesbitt (2011) claimed that they found a ring for RI storms where 85-GHz PCT \leq 250 K. However, in the 14-yr TRMM TC dataset that we examined, there are about 80% of RI cases with a 37-GHz cyan and pink ring and a 20-dBZ radar ring (when the inner core is covered by the PR swath). But most of these cases do not have a ring where 85-GHz PCT \leq 250 K, as shown in Figs. 16c and 17c. For comparison, Table 2 also shows that only 28 out of the 139 RI cases (about 20%) have a ring where 85-GHz PCT \leq 250 K within the TMI swath. The pink color in the 37-GHz color product roughly corresponds to 37-GHz PCT \leq 270 K, which is also roughly equivalent to 85-GHz PCT \leq 250 K, as you can see by

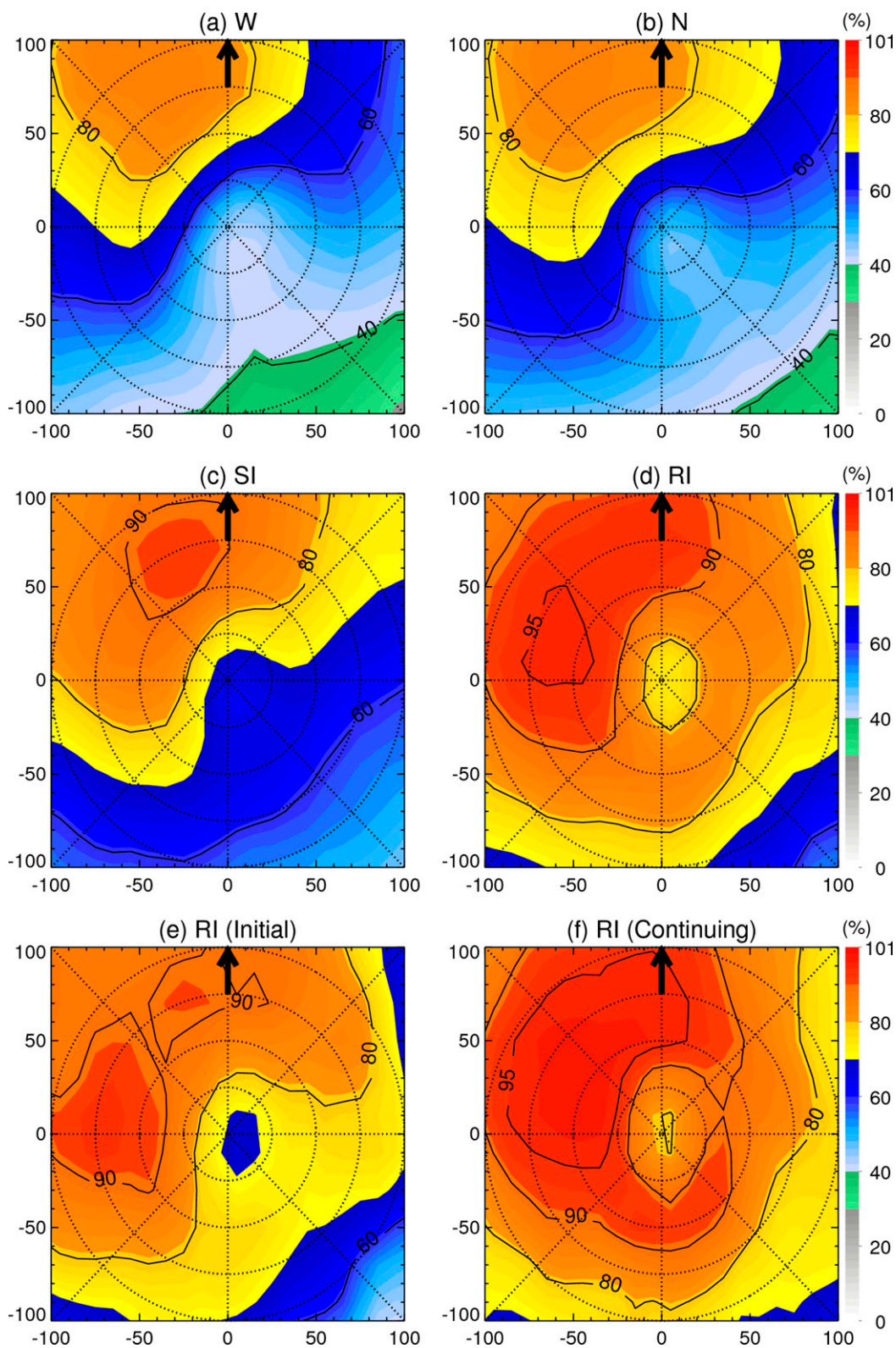


FIG. 15. As in Fig. 3, but for total precipitation degraded to the 37-GHz footprint size.

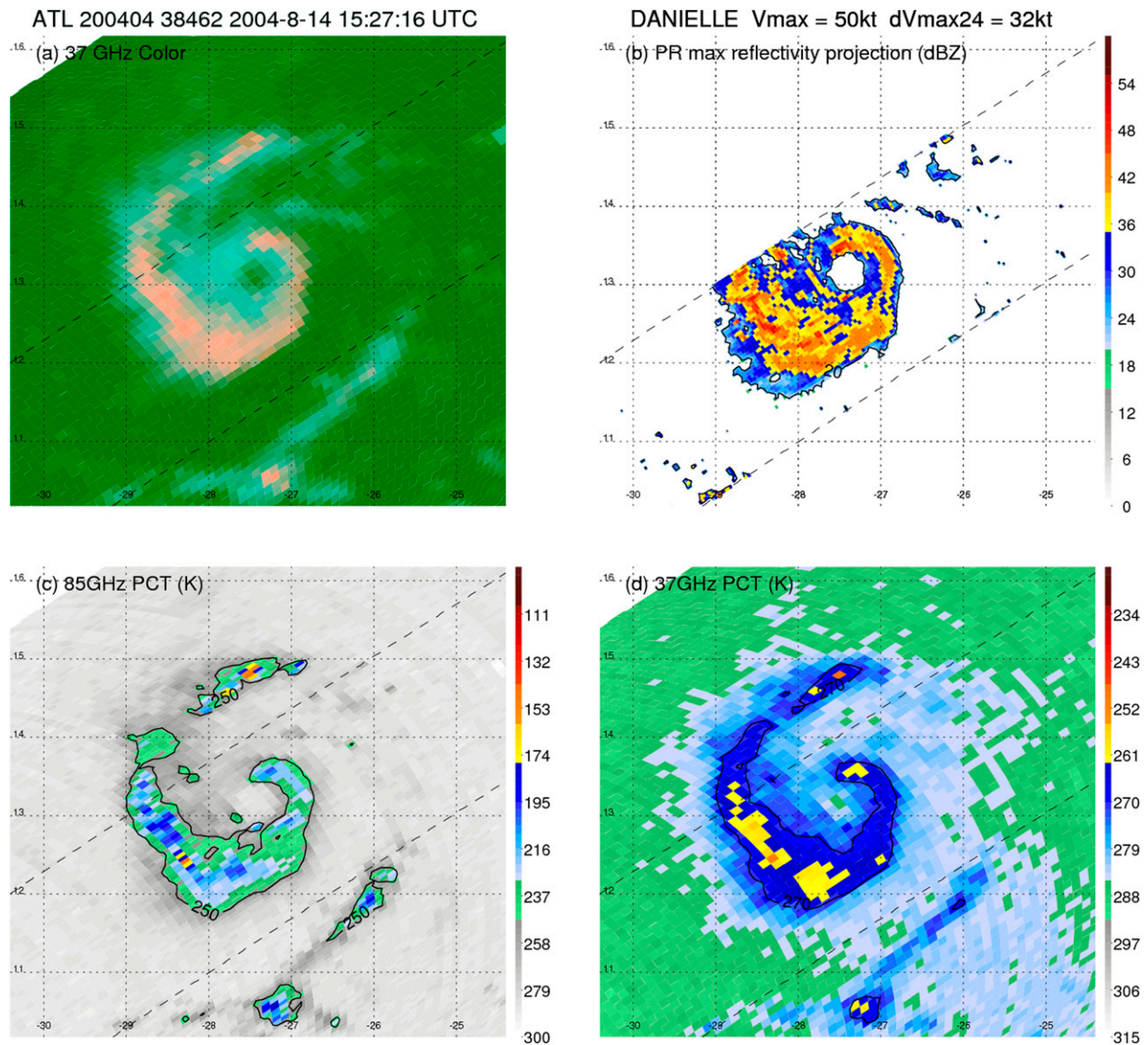


FIG. 16. An RI continuing case with a 37-GHz color cyan and pink ring observed by TRMM for Hurricane Danielle (2004) at 1527 UTC 14 August in the Atlantic (ATL) basin. (a) TMI 37-GHz color, (b) PR maximum reflectivity projection with 20-dBZ contour, (c) TMI 85-GHz PCT with 250-K contour, and (d) TMI 37-GHz PCT with 270-K contour. The V_{max} and 24-h future intensity change (dV_{max24}) are indicated at the top of (b).

comparing Fig. 16c with Fig. 16d and Fig. 17c with Fig. 17d. As pointed out in the introduction, the pink color simply indicates precipitation within ice, not necessarily deep convection, as indicated by Lee et al. (2002). Note that we define 85-GHz PCT by following Spencer et al. (1989) and 37-GHz PCT by following Cecil et al. (2002).

Using the 83 RI cases with a 37-GHz cyan and pink ring seen within the PR swath, Fig. 18 shows the composite shear-relative distributions of the percent occurrence of total precipitation, total-minus-shallow

precipitation, 37-GHz cyan and pink color, and 85-GHz PCT ≤ 250 K. Figures 18a,b are degraded to the 37-GHz footprint size in order to get the equivalent radar reflectivity field that the 37-GHz channel sees. An almost-closed 95% ring is seen in both Figs. 18a,c, indicating that the 37-GHz cyan and pink ring is essentially a radar echo ring containing at least 20-dBZ reflectivity. It is therefore concluded that the 37-GHz ring is precipitative. Note that the composite ring in Fig. 18c is not a 100% ring (even each of the 83 individual case has a ring) mainly

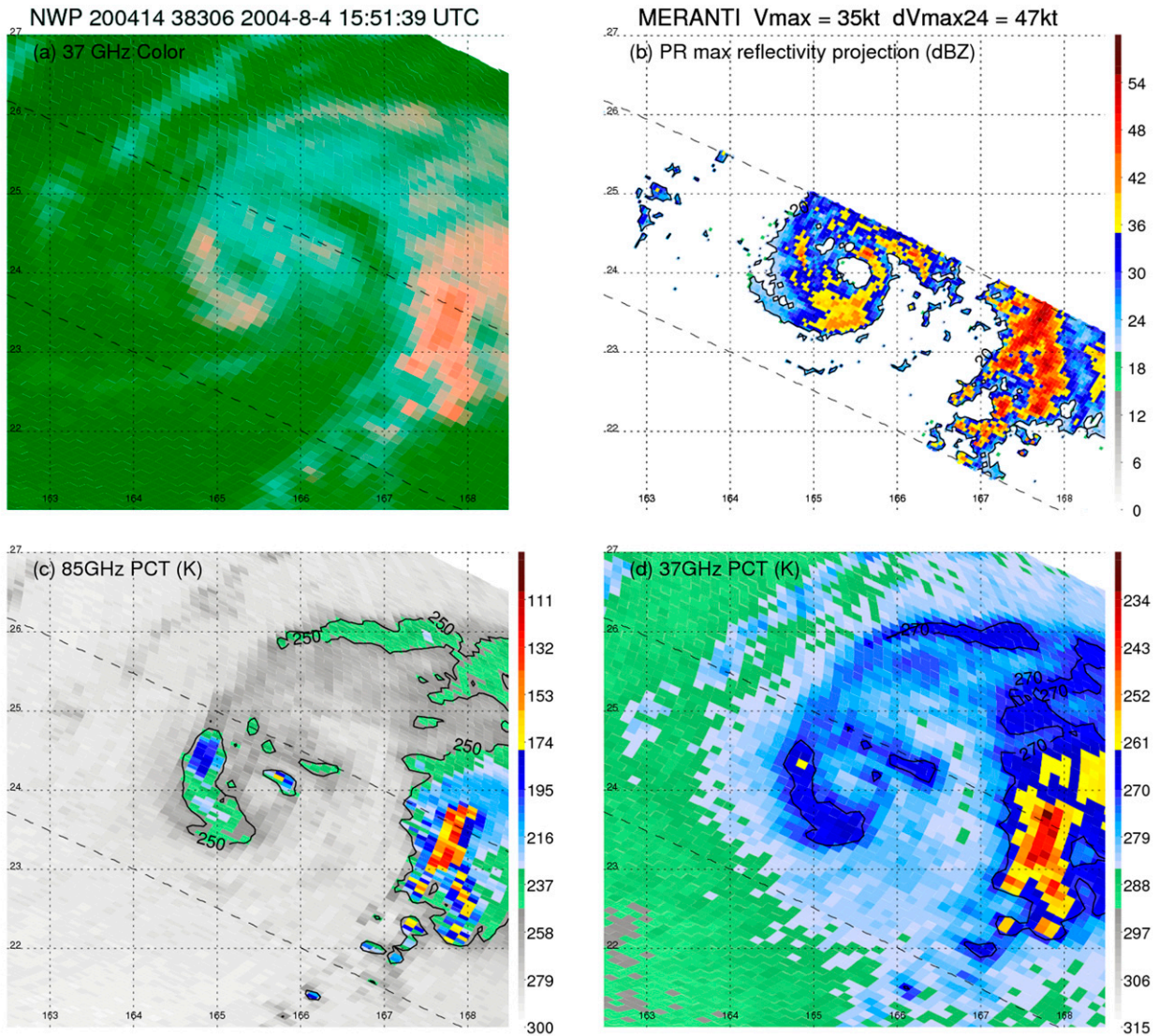


FIG. 17. As in Fig. 16, but for an RI initial case for Typhoon Meranti (2004) at 1551 UTC 4 August in the northwestern Pacific (NWP) basin.

because of the TC size difference and some small dislocation of the storm center. If shallow precipitation is excluded, the maximum value for the precipitative ring dropped to 40% (Fig. 18b). The 85-GHz PCT ≤ 250 K occurrence only has a 30% closed ring around the storm center (Fig. 18d), indicating that the so-called 85-GHz convective ring is not actually a good predictor for RI. If both shallow and moderate precipitation are excluded (only considering moderately deep and very deep precipitation), a ring of 5% occurrence is found (not shown), similar to the frequency of deep convection in ZJ14 (see their Fig. 8e). This implies that the 37-GHz ring feature in Kieper and Jiang (2012) is mostly contributed by shallow-moderate precipitation

and is thus reasonably denoted as precipitative. Interpretation of the 37-GHz cyan and pink ring feature in rapidly intensifying TCs will be further examined in an upcoming study.

5. Conclusions

Using 14 years of TRMM Precipitation Radar (PR) reflectivity data, shear-relative distributions of four types of precipitation-convection in different intensity categories of tropical cyclones (TCs) have been statistically quantified and compared in this study. With an emphasis on rapidly intensifying (RI) TCs, we analyzed 1139 TRMM PR overpasses of tropical

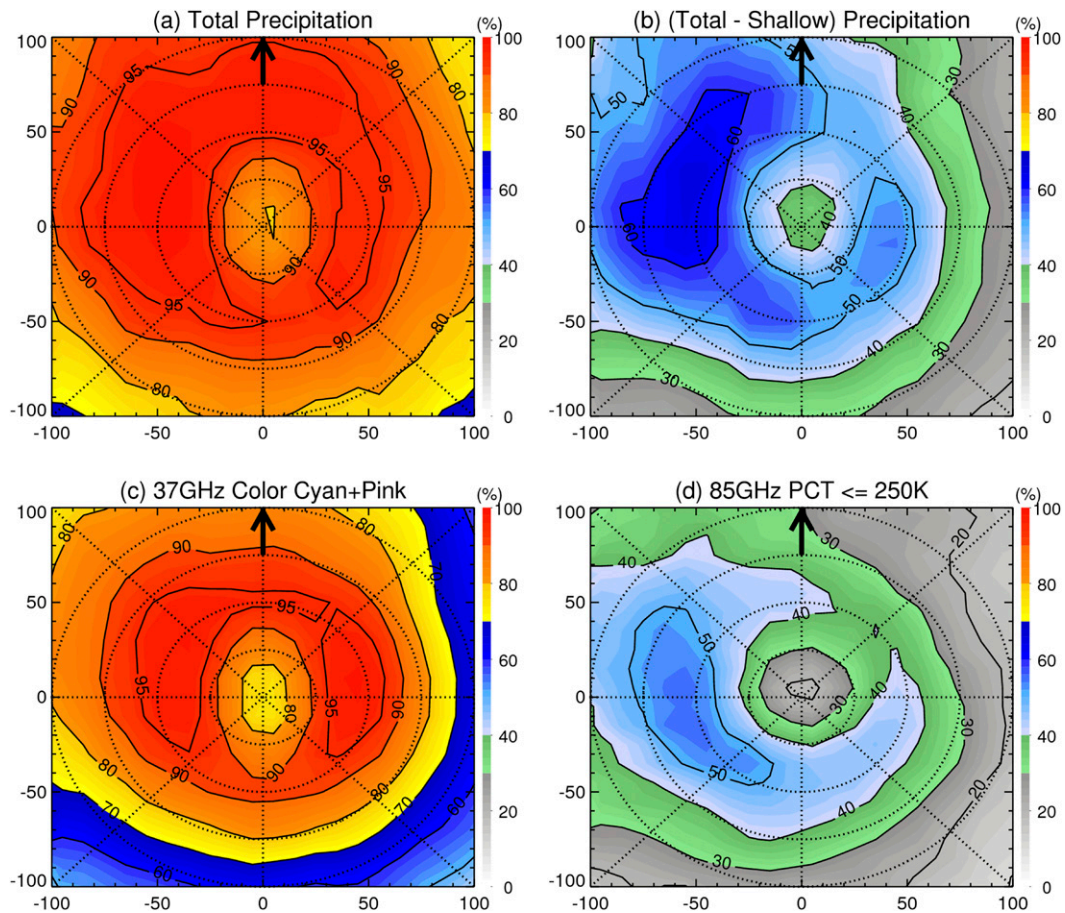


FIG. 18. Composite shear-relative distribution of the percent occurrence of (a) total precipitation (b) total minus shallow precipitation, (c) cyan and pink color on the 37-GHz color product, and (d) 85-GHz PCT ≤ 250 K for the 83 RI cases (including RI initial and RI continuing) with a 37-GHz cyan and pink ring seen within the PR swath (see Table 2). The black arrow represents the orientation of the vertical wind shear vector. The 25-, 50-, 75-, and 100-km radii are shown as dotted rings.

storms through category-2 hurricanes with at least moderately favorable environmental conditions.

Generally, shallow precipitation (defined as 20-dBZ radar echo top height < 6 km) is more widespread in RI than non-RI storms. A significant difference is observed between RI initial and slowly intensifying storms, as the RI initial category has a much higher frequency of shallow precipitation in all radial distances and shear-relative quadrants (Table 4; Figs. 2 and 6). This indicates that increased shallow precipitation surrounding the storm center is a first sign of RI and could be used as a predictor of the onset of RI.

Among the four types of precipitation defined in this study, moderate precipitation (20-dBZ radar echo top between 6 and 10 km) has the highest percent occurrence in TCs (about 27% overall; Table 4), followed by shallow precipitation (about 22% overall), moderately deep precipitation (about 3% overall), and very deep

precipitation (about 0.7% overall). Additionally, moderate precipitation contributes over 60% to both total volumetric rain and total latent heating, while the other three kinds of precipitation together account for less than 40% (Table 7).

The onset of RI also features more widespread moderate precipitation in all shear-relative quadrants than slowly intensifying, neutral, and weakening storms (Fig. 5; Table 4). Once the RI begins, the moderate precipitation frequency and its contributions to total volumetric rain and total latent heating continue to increase significantly and peak for RI continuing storms (Fig. 5; Table 7). The azimuthally averaged percent occurrence of moderately deep precipitation (20-dBZ radar echo between 10 and 14 km) is very similar in magnitude for storms at the onset of RI and those that are slowing intensifying (Fig. 2b), while storms during RI have a much higher occurrence of moderately deep precipitation. The

contribution to total volumetric rain from moderately deep precipitation also increases and becomes more symmetric around the center as RI continues.

Very deep precipitation (20-dBZ radar echo height ≥ 14 km) is quite rare in TCs and is more widespread in non-RI than RI storms (Fig. 3; Table 4). The maximum frequencies of both moderately deep and very deep precipitation are located closer to the storm center in RI storms than in non-RI storms. Although very deep precipitation accounts for a disproportionate amount of total volumetric rain and total latent heat within the inner core, its absolute percent contribution decreases in order from slowly intensifying, neutral, weakening, RI initial, to RI continuing storms (Table 7).

It is found that the contribution to total volumetric rain and total latent heating from the shallow–moderate precipitation in the inner core is greater in RI initial and continuing storms than non-RI storms, while the opposite is true for moderately to very deep precipitation (Table 7). This implies that the shallow–moderate precipitation is more important in initiating and maintaining RI. This is consistent with ZJ14 and other satellite-based statistical studies (e.g., Jiang 2012; Jiang and Ramirez 2013) showing that it is not the deep convection but the widespread and symmetric rainfall that is more important to RI. However, this is inconsistent with previous observational case studies (e.g., Reasor et al. 2009; Guimond et al. 2010; Molinari and Vollaro 2010; Nguyen and Molinari 2012; Reasor and Eastin 2012; Stevenson et al. 2014; Rogers et al. 2015; Susca-Lopata et al. 2015), which emphasized the role of asymmetric very deep convection in RI. As mentioned in section 4, most of these observational case studies are biased toward the ending period of RI, while the three studies about Hurricane Earl (2010) focused on deep convection before RI while the storm was in the slowly intensifying stage. Here we argue that RI is more likely triggered by the increase of shallow–moderate precipitation and the appearance of more moderately to very deep convection in the middle of RI is more likely a response or positive feedback to changes in the vortex that occur earlier in the slowly intensifying period to the beginning of the RI period. The specific mechanism of how shallow–moderate precipitation initiates RI is unknown, but a hypothesized conceptual model is given in Fig. 14. It is proposed that the increased shallow–moderate precipitation at the onset of RI might be linked with the moistening, vortex alignment, axisymmetrization, and more latent heat release. Further studies are needed in this direction.

Another interesting finding of this study is that although the downshear-left quadrant is favored for all types of precipitation for weakening, neutral, and slowly intensifying storms, consistent with previous studies for TCs in general (e.g., Corbosiero and Molinari 2002, 2003; Chen et al. 2006; Cecil 2007; Hince and Houze 2012), the shear-relative distributions for RI storms are very different. A cyclonic rotation of peaks from shallow (downshear right) to moderate (downshear left) to moderately and very deep precipitation (upshear left) follows the tangential wind direction around the TC center and may be an indicator of the vortex rapidly strengthening.

A ring of almost 90% occurrence of total precipitation is found for storms in the middle of RI (Fig. 14f). After selecting the RI cases with a 37-GHz cyan and pink ring seen in the PR swath, Fig. 18 indicates that a total precipitation ring is closely analogous to the cyan and pink ring in the 37-GHz color product defined by Kieper and Jiang (2012) that is a very good predictor for RI. The ring is mostly contributed by shallow–moderate precipitation and is thus reasonably denoted as precipitative. The ring indicates a very high degree of symmetry of shallow–moderate precipitation. Shallow precipitation alone contributes about 40%–50% of the ring (Fig. 18b). A ring of only 20%–30% occurrence of 85-GHz PCT ≤ 250 K is found for RI cases, indicating that the 85-GHz convective ring claimed by Harnos and Nesbitt (2011) is not a good predictor of RI (Table 2; Fig. 18d). Jiang and Ramirez (2013) found that the total volumetric rain and total raining area in the inner-core region is much higher in RI storms than non-RI storms. They concluded that high total raining area and total volumetric rain in the inner core are necessary conditions of RI. However, by further separating RI into RI initial and continuing categories, this study finds that higher volumetric rain in the inner core appears only during RI but not at the onset of RI, suggesting that it is a symptom rather than an indicator of the onset of RI.

Acknowledgments. The authors would like to acknowledge Joseph P. Zagrodnik for the construction of the dataset, and Drs. Tie Yuan and Chuntao Liu for helping on TRMM data processing. The authors also give thanks to Dr. Ed Zipser and two anonymous reviewers for their very important and useful comments, which helped improve the manuscript substantially. This work was supported financially by the NASA Earth and Space Science Fellowship (NESSF) Award NNX11AL66H and the Dissertation Year Fellowship of FIU. Additional support for this study was also provided by NASA New Investigator Program (NIP) Award NNX10AG55G, NASA Hurricane Science Research Program (HSRP) Grant NNX10AG34G, and NOAA

Joint Hurricane Testbed (JHT) Grants NA11OAR4310193, NA13OAR4590191, and NA15OAR4590199. The authors thank Drs. Ramesh Kakar and Ming-Ying Wei (NASA headquarters) and Dr. Chris Landsea (NOAA JHT program) for their continued support.

REFERENCES

- Black, M. L., J. F. Gamache, F. D. Marks Jr., C. E. Samsury, and H. E. Willoughby, 2002: Eastern Pacific Hurricanes Jimena of 1991 and Olivia of 1994: The effect of vertical shear on structure and intensity. *Mon. Wea. Rev.*, **130**, 2291–2312, doi:10.1175/1520-0493(2002)130<2291:EPHJOA>2.0.CO;2.
- Cecil, D. J., 2007: Satellite-derived rain rates in vertically sheared tropical cyclones. *Geophys. Res. Lett.*, **34**, L02811, doi:10.1029/2006GL027942.
- , and E. J. Zipser, 2002: Reflectivity, ice scattering, and lightning characteristics of hurricane eyewalls and rainbands. Part II: Intercomparison of observations. *Mon. Wea. Rev.*, **130**, 785–801, doi:10.1175/1520-0493(2002)130<0785:RISALC>2.0.CO;2.
- , —, and S. W. Nesbitt, 2002: Reflectivity, ice scattering, and lightning characteristics of hurricane eyewalls and rainbands. Part I: Quantitative description. *Mon. Wea. Rev.*, **130**, 769–784, doi:10.1175/1520-0493(2002)130<0769:RISALC>2.0.CO;2.
- Chen, H., and S. G. Gopalakrishnan, 2015: A study on the asymmetric rapid intensification of Hurricane Earl (2010) using the HWRF system. *J. Atmos. Sci.*, **72**, 531–550, doi:10.1175/JAS-D-14-0097.1.
- Chen, S. S., J. A. Knaff, and F. D. Marks, 2006: Effects of vertical wind shear and storm motion on tropical cyclone rainfall asymmetries deduced from TRMM. *Mon. Wea. Rev.*, **134**, 3190–3208, doi:10.1175/MWR3245.1.
- Corbosiero, K. L., and J. Molinari, 2002: The effects of vertical wind shear on the distribution of convection in tropical cyclones. *Mon. Wea. Rev.*, **130**, 2110–2123, doi:10.1175/1520-0493(2002)130<2110:TEOVWS>2.0.CO;2.
- , and —, 2003: The relationship between storm motion, vertical wind shear, and convective asymmetries in tropical cyclones. *J. Atmos. Sci.*, **60**, 366–376, doi:10.1175/1520-0469(2003)060<0366:TRBSMV>2.0.CO;2.
- Fierro, A., J. Simpson, M. A. LeMone, J. M. Straka, and B. F. Smull, 2009: On how hot towers fuel the Hadley cell: An observational and modeling study of line-organized convection in the equatorial trough from TOGA COARE. *J. Atmos. Sci.*, **66**, 2730–2746, doi:10.1175/2009JAS3017.1.
- Gottelman, A., M. L. Salby, and F. Sassi, 2002: Distribution and influence of convection in the tropical tropopause region. *J. Geophys. Res.*, **107**, 4080, doi:10.1029/2001JD001048.
- Guimond, S. R., G. M. Heymsfield, and F. J. Turk, 2010: Multiscale observations of Hurricane Dennis (2005): The effects of hot towers on rapid intensification. *J. Atmos. Sci.*, **67**, 633–654, doi:10.1175/2009JAS3119.1.
- Harnos, D. S., and S. W. Nesbitt, 2011: Convective structure in rapidly intensifying tropical cyclones as depicted by passive microwave measurements. *Geophys. Res. Lett.*, **38**, L07805, doi:10.1029/2011GL047010.
- Hence, D. A., and R. A. Houze Jr., 2011: Vertical structure of hurricane eyewalls as seen by the TRMM Precipitation Radar. *J. Atmos. Sci.*, **68**, 1637–1652, doi:10.1175/2011JAS3578.1.
- , and —, 2012: Vertical structure of tropical cyclone rainbands as seen by the TRMM Precipitation Radar. *J. Atmos. Sci.*, **69**, 2644–2661, doi:10.1175/JAS-D-11-0323.1.
- Hendricks, E. A., M. T. Montgomery, and C. A. Davis, 2004: The role of “vortical” hot towers in the formation of tropical cyclone Diana (1984). *J. Atmos. Sci.*, **61**, 1209–1232, doi:10.1175/1520-0469(2004)061<1209:TROVHT>2.0.CO;2.
- , M. S. Peng, B. Fu, and T. Li, 2010: Quantifying environmental control on tropical cyclone intensity change. *Mon. Wea. Rev.*, **138**, 3243–3271, doi:10.1175/2010MWR3185.1.
- Houze, R. A., Jr., W.-C. Lee, and M. M. Bell, 2009: Convective contribution to the genesis of Hurricane Ophelia (2005). *Mon. Wea. Rev.*, **137**, 2778–2800, doi:10.1175/2009MWR2727.1.
- Iguchi, T., T. Kozu, R. Meneghini, J. Awaka, and K. I. Okamoto, 2000: Rain-profiling algorithm for the TRMM Precipitation Radar. *J. Appl. Meteor.*, **39**, 2038–2052, doi:10.1175/1520-0450(2001)040<2038:RPAFTT>2.0.CO;2.
- , —, J. Kwiatkowski, R. Meneghini, J. Awaka, and K. I. Okamoto, 2009: Uncertainties in the rain profiling algorithm for the TRMM Precipitation Radar. *J. Meteor. Soc. Japan*, **87A**, 1–30, doi:10.2151/jmsj.87A.1.
- Jiang, H., 2012: The relationship between tropical cyclone intensity change and the strength of inner-core convection. *Mon. Wea. Rev.*, **140**, 1164–1176, doi:10.1175/MWR-D-11-00134.1.
- , and E. M. Ramirez, 2013: Necessary conditions for tropical cyclone rapid intensification as derived from 11 years of TRMM data. *J. Climate*, **26**, 6459–6470, doi:10.1175/JCLI-D-12-00432.1.
- , and C. Tao, 2014: Contribution of tropical cyclones to global deep convection. *J. Climate*, **27**, 4313–4336, doi:10.1175/JCLI-D-13-00085.1.
- , C. Liu, and E. J. Zipser, 2011: A TRMM-based tropical cyclone cloud and precipitation feature database. *J. Appl. Meteor. Climatol.*, **50**, 1255–1274, doi:10.1175/2011JAMC2662.1.
- Johnson, R. H., T. M. Rickenbach, S. A. Rutledge, P. E. Ciesielski, and W. H. Schubert, 1999: Trimodal characteristics of tropical convection. *J. Climate*, **12**, 2397–2418, doi:10.1175/1520-0442(1999)012<2397:TCOTC>2.0.CO;2.
- Kaplan, J., and M. DeMaria, 2003: Large-scale characteristics of rapidly intensifying tropical cyclones in the North Atlantic basin. *Wea. Forecasting*, **18**, 1093–1108, doi:10.1175/1520-0434(2003)018<1093:LCORIT>2.0.CO;2.
- , —, and J. A. Knaff, 2010: A revised tropical cyclone rapid intensification index for the Atlantic and eastern North Pacific basins. *Wea. Forecasting*, **25**, 220–241, doi:10.1175/2009WAF2222280.1.
- Kelley, O. A., 2008: The association of tall eyewall convection with tropical cyclone wind intensification. Ph.D. dissertation, George Mason University, 341 pp.
- , J. Stout, and J. B. Halverson, 2004: Tall precipitation cells in tropical cyclone eyewalls are associated with tropical cyclone intensification. *Geophys. Res. Lett.*, **31**, L24112, doi:10.1029/2004GL021616.
- Kieper, M. E., and H. Jiang, 2012: Predicting tropical cyclone rapid intensification using the 37 GHz ring pattern identified from passive microwave measurements. *Geophys. Res. Lett.*, **39**, L13804, doi:10.1029/2012GL052115.
- Lee, T. F., F. J. Turk, J. Hawkins, and K. Richardson, 2002: Interpretation of TRMM TMI images of tropical cyclones. *Earth Interact.*, **6**, 1–17, doi:10.1175/1087-3562(2002)006<0001:IOOTTO>2.0.CO;2.

- Liu, C., and E. J. Zipser, 2005: Global distribution of convection penetrating the tropical tropopause. *J. Geophys. Res.*, **110**, D23104, doi:10.1029/2005JD006063.
- Marks, F. D., and L. K. Shay, 1998: Landfalling tropical cyclones: Forecast problems and associated research opportunities. *Bull. Amer. Meteor. Soc.*, **79**, 305–323, doi:10.1175/1520-0477(1998)079<0305:LTCFPA>2.0.CO;2.
- Merrill, R. T., 1988: Environmental influences on hurricane intensification. *J. Atmos. Sci.*, **45**, 1678–1687, doi:10.1175/1520-0469(1988)045<1678:EIOHI>2.0.CO;2.
- Molinari, J., and D. Vollaro, 2010: Rapid intensification of a sheared tropical storm. *Mon. Wea. Rev.*, **138**, 3869–3885, doi:10.1175/2010MWR3378.1.
- Montgomery, M. T., and R. K. Smith, 2011: Paradigms for tropical cyclone intensification. *Quart. J. Roy. Meteor. Soc.*, **137**, 1–31.
- , M. E. Nicholls, T. A. Cram, and A. B. Saunders, 2006: A vortical hot tower route to tropical cyclogenesis. *J. Atmos. Sci.*, **63**, 355–386, doi:10.1175/JAS3604.1.
- Nesbitt, S. W., E. J. Zipser, and D. J. Cecil, 2000: A census of precipitation features in the tropics using TRMM: Radar, ice scattering, and lightning observations. *J. Climate*, **13**, 4087–4106, doi:10.1175/1520-0442(2000)013<4087:ACOPFI>2.0.CO;2.
- Nguyen, L. T., and J. Molinari, 2012: Rapid intensification of a sheared, fast-moving hurricane over the Gulf Stream. *Mon. Wea. Rev.*, **140**, 3361–3378, doi:10.1175/MWR-D-11-00293.1.
- Nguyen, V. S., R. K. Smith, and M. T. Montgomery, 2008: Tropical-cyclone intensification and predictability in three dimensions. *Quart. J. Roy. Meteor. Soc.*, **134**, 563–582, doi:10.1002/qj.235.
- Nolan, D. S., and L. D. Grasso, 2003: Nonhydrostatic, three-dimensional perturbations to balanced, hurricane-like vortices. Part II: Symmetric response and nonlinear simulations. *J. Atmos. Sci.*, **60**, 2717–2745, doi:10.1175/1520-0469(2003)060<2717:NTPTBH>2.0.CO;2.
- , Y. Moon, and D. P. Stern, 2007: Tropical cyclone intensification from asymmetric convection: Energetics and efficiency. *J. Atmos. Sci.*, **64**, 3377–3405, doi:10.1175/JAS3988.1.
- Ooyama, K., 1969: Numerical simulation of the life cycle of tropical cyclones. *J. Atmos. Sci.*, **26**, 3–40, doi:10.1175/1520-0469(1969)026<0003:NSOTLC>2.0.CO;2.
- Park, M.-S., and R. L. Elsberry, 2013: Latent heating and cooling rates in developing and nondeveloping tropical disturbances during TCS-08: TRMM PR versus ELDORA retrievals. *J. Atmos. Sci.*, **70**, 15–35, doi:10.1175/JAS-D-12-083.1.
- Reasor, P. D., and M. D. Eastin, 2012: Rapidly intensifying Hurricane Guillermo (1997). Part II: Resilience in shear. *Mon. Wea. Rev.*, **140**, 425–444, doi:10.1175/MWR-D-11-00080.1.
- , M. T. Montgomery, and L. F. Bosart, 2005: Mesoscale observations of the genesis of Hurricane Dolly (1996). *J. Atmos. Sci.*, **62**, 3151–3171, doi:10.1175/JAS3540.1.
- , M. D. Eastin, and J. F. Gamache, 2009: Rapidly intensifying Hurricane Guillermo (1997). Part I: Low-wavenumber structure and evolution. *Mon. Wea. Rev.*, **137**, 603–631, doi:10.1175/2008MWR2487.1.
- , R. F. Rogers, and S. Lorsolo, 2013: Environmental flow impacts on tropical cyclone structure diagnosed from airborne Doppler radar composites. *Mon. Wea. Rev.*, **141**, 2949–2969, doi:10.1175/MWR-D-12-00334.1.
- Reynolds, R. W., T. M. Smith, C. Liu, D. B. Chelton, K. S. Casey, and M. G. Schlax, 2007: Daily high-resolution-blended analyses for sea surface temperature. *J. Climate*, **20**, 5473–5496, doi:10.1175/2007JCLI1824.1.
- Riehl, H., and J. S. Malkus, 1958: On the heat balance in the equatorial trough zone. *Geophysica*, **6**, 503–538.
- Rogers, R. F., 2010: Convective-scale structure and evolution during a high-resolution simulation of tropical cyclone rapid intensification. *J. Atmos. Sci.*, **67**, 44–70, doi:10.1175/2009JAS3122.1.
- , S. S. Chen, J. Tenerelli, and H. E. Willoughby, 2003: A numerical study of the impact of vertical shear on the distribution of rainfall in Hurricane Bonnie (1998). *Mon. Wea. Rev.*, **131**, 1577–1599, doi:10.1175/2546.1.
- , P. D. Reasor, and S. Lorsolo, 2013: Airborne Doppler observations of the inner-core structural differences between intensifying and steady-state tropical cyclones. *Mon. Wea. Rev.*, **141**, 2970–2991, doi:10.1175/MWR-D-12-00357.1.
- , —, and J. A. Zhang, 2015: Multiscale structure and evolution of Hurricane Earl (2010) during rapid intensification. *Mon. Wea. Rev.*, **143**, 536–562, doi:10.1175/MWR-D-14-00175.1.
- Shapiro, L. J., and H. E. Willoughby, 1982: The response of balanced hurricanes to local sources of heat and momentum. *J. Atmos. Sci.*, **39**, 378–394, doi:10.1175/1520-0469(1982)039<0378:TROBHT>2.0.CO;2.
- Shige, S., Y. N. Takayabu, W.-K. Tao, and D. E. Johnson, 2004: Spectral retrieval of latent heating profiles from TRMM PR data. Part I: Development of a model-based algorithm. *J. Appl. Meteor.*, **43**, 1095–1113, doi:10.1175/1520-0450(2004)043<1095:SRLOHP>2.0.CO;2.
- , —, —, and C.-L. Shie, 2007: Spectral retrieval of latent heating profiles from TRMM PR data. Part II: Algorithm improvement and heating estimates over tropical ocean regions. *J. Appl. Meteor. Climatol.*, **46**, 1098–1124, doi:10.1175/JAM2510.1.
- Simmons, A., S. Uppala, D. Dee, and S. Kobayashi, 2007: ERA-Interim: New ECMWF reanalysis products from 1989 onwards. *ECMWF Newsletter*, No. 110, ECMWF, Reading, United Kingdom, 26–35.
- Simpson, R., 1978: On the computation of equivalent potential temperature. *Mon. Wea. Rev.*, **106**, 124–130, doi:10.1175/1520-0493(1978)106<0124:OTCOEP>2.0.CO;2.
- Spencer, R. W., H. M. Goodman, and R. E. Hood, 1989: Precipitation retrieval over land and ocean with the SSM/I: Identification and characteristics of the scattering signal. *J. Atmos. Oceanic Technol.*, **6**, 254–273, doi:10.1175/1520-0426(1989)006<0254:PROLAO>2.0.CO;2.
- Stevenson, S. N., K. L. Corbosiero, and J. Molinari, 2014: The convective evolution and rapid intensification of Hurricane Earl (2010). *Mon. Wea. Rev.*, **142**, 4364–4380, doi:10.1175/MWR-D-14-00078.1.
- Susca-Lopata, G., J. Zawislak, E. J. Zipser, and R. F. Rogers, 2015: The role of observed environmental conditions and precipitation evolution in the rapid intensification of Hurricane Earl (2010). *Mon. Wea. Rev.*, **143**, 2207–2223, doi:10.1175/MWR-D-14-00283.1.
- Tao, C., and H. Jiang, 2013: Global distribution of hot towers in tropical cyclones based on 11-yr TRMM data. *J. Climate*, **26**, 1371–1386, doi:10.1175/JCLI-D-12-00291.1.
- Vigh, J. L., and W. H. Schubert, 2009: Rapid development of the tropical cyclone warm core. *J. Atmos. Sci.*, **66**, 3335–3350, doi:10.1175/2009JAS3092.1.
- Wang, Y., and C.-C. Wu, 2004: Current understanding of tropical cyclone structure and intensity changes—A review. *Meteor. Atmos. Phys.*, **87**, 257–278, doi:10.1007/s00703-003-0055-6.

- Willoughby, H. E., J. A. Clos, and M. G. Shoreibah, 1982: Concentric eye walls, secondary wind maxima, and the development of the hurricane vortex. *J. Atmos. Sci.*, **39**, 395–411, doi:[10.1175/1520-0469\(1982\)039<0395:CEWSWM>2.0.CO;2](https://doi.org/10.1175/1520-0469(1982)039<0395:CEWSWM>2.0.CO;2).
- Wingo, M. T., and D. J. Cecil, 2010: Effects of vertical wind shear on tropical cyclone precipitation. *Mon. Wea. Rev.*, **138**, 645–662, doi:[10.1175/2009MWR2921.1](https://doi.org/10.1175/2009MWR2921.1).
- Zagrodnik, J. P., and H. Jiang, 2014: Rainfall, convection, and latent heating distributions in rapidly intensifying tropical cyclones. *J. Atmos. Sci.*, **71**, 2789–2809, doi:[10.1175/JAS-D-13-0314.1](https://doi.org/10.1175/JAS-D-13-0314.1).
- Zhang, D.-L., and H. Chen, 2012: Importance of the upper-level warm core in the rapid intensification of a tropical cyclone. *Geophys. Res. Lett.*, **39**, L02806, doi:[10.1029/2011GL050578](https://doi.org/10.1029/2011GL050578).